Investigation of Oxy-Fuel Combustion in a Circulating Fluidized Bed Boiler in Ansys Fluent® Without Incorporation of User Defined Functions.

Jakob Bo Jensen & Nicolai Ranum

AAU Energy, TEPE4-1002, 2024-06

Master's Thesis

AALBORG UNIVERSITY
STUDENT REPORT

Department of Energy
Aalborg University
www.energy.aau.dk

Title:
Investigation of Oxy-Fuel Combustion in a Circulating Fluidized Bed Boiler in Ansys FLUENT® Without Incorporation of User Defined Functions.

Theme:
Master's Thesis

Project Period:
Spring Semester 2024

Project Group:
TEPE4-1002

Participants:
Jakob Bo Jensen
Nicolai Ranum

Supervisor:
Chungen Yin

Copies: 1

Page Numbers: 81

Date of Completion:
31. May 2024

Abstract:

This project investigates the capability of the Ansys FLUENT® software, within the field of combustion and multiphase flow, without the incorporation of User Defined Functions (UDF). Additionally, different particle tracking methods/models are compared, namely the Discrete Element Method (DEM) and the standard Kinetic Theory of Granular Flow (KTGF) model. The KTGF was found to be easier implemented while requiring less computational time compared to the DEM, which was concluded to require 20% longer computational time. Eddy-Dissipation was chosen in favor of Eddy-dissipation/Finite rate due to the slow kinetic rates, as a result the volatiles did not combust. Four simulations have been compared with the experimental data, where simulation one showed a mean deviation of 47%, while simulation four had a deviation of 21.6%. Lastly, it was concluded that the FLUENT® software is able to deliver reasonable results in multiphase-combustion simulations without the use of UDFs, and that the deviations are a result of insufficient computational time and mesh quality, rather than a lack of UDFs.

Summary

This project aims to investigate oxy-fuel combustion in a Circulating Fluidized Bed (CFB) boiler using numerical simulations. The investigation of CFB boilers is of special interest, since the CFB technology offers advantages in terms of fuel flexibility and emission control. A literature study reveals that publications on the investigation of CFB boilers are plentiful. Most of these investigate hydrodynamic behaviour and combustion using 3D simulations, while few investigate 2D simulations. Multiple CFD software are used in these investigations, however, Ansys FLUENT® is the most widely used. In many papers it has been deemed necessary to implement User Defined Functions (UDF), in order to combine multiphase models and combustion models. This can often be a very challenging and time consuming task, which makes it relevant to investigate the modelling of CFB boilers without the use of UDFs. Having determined the importance of combustion simulations in CFB boilers the problem statement is

How can combustion combined with the multiphase flow existing in a CFB be modelled and simulated in Ansys* Fluent® *without the incorporation of UDFs?

The CFB boiler in this project is based on the experimental setup by Li et al. [1], which is a 100 kW oxy-fuel CFB boiler, where the geometry is simplified and detailed in [2]. The project utilizes the simplified geometry by Gu, Zhong, and Yu [2] which includes; furnace, downcomer, riser, cyclone separator and a loop seal. Using a full closed loop geometry, eliminates the need for UDFs to model recirculation. Several settings and criteria are explained in Chapter 3, this includes settings for mesh and the models active in FLUENT®, with a summarized table at the end of the chapter. The mathematical theory in FLUENT® is described thoroughly for the various models, this includes; gas-solid flow, turbulence and energy. Additionally, the discretization scheme used in the FLUENT® software is explained. The combustion processes are explained in detail, including how FLUENT® handles combustion reactions using finite rate calculations. Additionally, a brief explanation of the devolatilization of coal is provided. Tables present the proximate and ultimate analyses, along with further information on the properties of coal. File injections for the particulate phase are used in designated areas, to inject the desired mass of particles, which correspond to the volume fraction used in [2]. The GCI study was performed using three different meshes, where a deviation of 7.35% on the coarse grid was observed and a deviation of 3.45% on the fine grid was obtained, not considering the safety factor. Two cases are created; a case with multiphase and turbulence enabled, and a case with multiphase turbulence, energy and combustion enabled. In case one the impact on particle distribution of the models Kinetic Theory of Granular Flow (KTGF) and Discrete Element Method (DEM) are compared, and it becomes evident that DEM overestimates the particle

collision force, evidently resulting in a larger distribution throughout the domain. While the DEM is generally preferred in high particle loading cases, it is both more challenging to implement and resulting computational time increased by 20%. Enabling all the models in FLUENT® in case two, proved to be troublesome. A relatively low temperature was observed throughout the domain, considering combustion was enabled. It was determined that the low temperature was due to the volatiles not combusting. This was caused by the slow reaction kinetics in the Arrhenius equation, that governs the finite rate chemistry, and was inadequate when initializing the temperature to 1123 K. To overcome this, the Finite Rate/Eddy Dissipation model was deactivated, and the Eddy Dissipation model was used alone. Using the Eddy Dissipation model, the reaction kinetics are neglected, since the reactions are assumed to be governed by turbulent mixing, rather than reaction rates. Simulating 30 s of flow time with a coarser mesh, and Eddy Dissipation active, resulted in a higher measured temperature throughout the domain, indicating that simulation time is crucial in combustion simulations. When comparing the temperature profiles with that of the experimental data, the largest mean deviation was 47.7% while the smallest deviation was only 21.6%. Lastly, it is concluded that Ansys Fluent is capable of delivering reasonable results in multiphase-combustion simulations, without the use of UDFs. The deviations of the simulations are not caused by a lack of UDFs, but rather a result of the mesh and limited computational time.

Preface

This master's thesis in Thermal Energy and Process Engineering on Aalborg university is written by group TEPE4-1002, consisting of Jakob Bo Jensen and Nicolai Ranum. The project period span from the 5th of February to the 31st of May 2024. The project focuses on computational fluid dynamics simulations of a circulating fluidized bed boiler, comparing the particulate phase distribution across different models and aiming to validate the combustion process in the boiler. The project group would like to extend their gratitude to supervisor Chungen Yin for their assistance and feedback throughout the project period.
For this paper following software have been used:

- Overleaf LaTeX – For text formatting
- MathWorks MATLAB – For calculations and graphs
- Ansys Fluent® – For CFD simulations and Meshing
- Ansys Spaceclaim – For 3D geometry
- InkScape – For drawings and flowcharts
- Maple – For calculations

Reading Guide

The paper contains a nomenclature with an overview of the used abbreviations and symbols arranged alphabetically. The main part of the project consists of chapters and sections with assigned numbering. Appendices are labelled with a letter. Figures, Tables and Equations are assigned numbers after which order they appear in a chapter.
The Vancouver method is used for referencing. With the number of the reference stating the order it appears in the project. The first reference written as [1]. In the bibliography, the reference number appears along with relevant information on the source and accompanying ISBN, doi or url. If a section is based on a source, the reference appears after the period. Similarly for a sentence the source is stated at the end of the sentence before the period and for numbers its stated immediately after the given number. Additionally, if a chapter or section is based largely on a single or multiple sources, this is stated at the beginning of the corresponding chapter or section.

Jakob Bo Jensen
<jjense19@student.aau.dk>

Nicolai Ranum
<nranum19@student.aau.dk>

Nomenclature

Abbreviation	Description
AR	As Received
CAS	Chinese Academy of Science
CFB	Circulating Fludized Bed
CFD	Computational Fluid Dynamics
CFL	Courant-Friedrichs-Lewy
DDPM	Dense Discrete Phase Model
DEM	Discrete Element Method
DPM	Discrete Phase Model
EU	European Union
GCI	Grid Convergence Index
GHG	Green House Gas
HCV	Higher Calorific Value
IA	Interfacial Area
Le	Lewis number
LES	Large Eddy Simulation
PC	Pulverized Coal
Pe	Peclet number
Pr	Prandtl Number
RANS	Reynolds-Averaged-Navier-Stokes
Sc	Schmidt Number
SGS	Subgrid-Scale
TCI	Turbulence-Chemistry Interaction
UDF	User Defined Function

Symbol	Description	SI Unit
C_d	Drag coefficient	[-]
d_p	Particle diameter	[m]
e	Internal Energy	[J]
$\vec{e}$	Unit vector from particle	[-]
f	Solution and exact solution	[-]
g	Gravitational acceleration	$[m/s^2]$
h	Enthalpy	[J]
h_i	Grid spacing	$[m^3]$
k	Reaction rate	[mol/s]
k	Turbulent kinetic energy	[J]
k	Thermal conductivity	$[W/m \cdot K]$
k	Spring constant	[-]
k_{eff}	Effective thermal conductivity	$[W/m \cdot K]$
m	Mass	[kg]
$\dot{m}$	Mass flow	[kg/s]
p	Pressure	[Pa]
s	Sign function	[-]
t	Time	[s]
u	Velocity in x direction	[m/s]
v	Velocity in y direction	[m/s]
w	Velocity in z direction	[m/s
A	Constant related to k-ϵ	[-]
A	Area	$[m^2]$
A	Pre-exponential factor	[-]
C	Rotational drag coefficient	[-]
C_d	Drag coefficient	[-]
Co	Courant Number	[-]
$D_{i,m}$	Mixture averaged diffusion coefficient	[-]
E	Activation energy	[J]
$\vec{F}$	Force	[N]
I_p	Momentum of inertia for a spherical particle	$[kg \cdot m^2]$
J	Diffusion flux	$[mol/m^2 \cdot s]$
K_{DPM}	Averaged particle interphase momentum exchange	$[kg \cdot m/s]$
R	Net rate of production	[M/s]
R	Universal gas constant	$[J/mol \cdot K]$
S	Source term	$[-]$
$\vec{T}$	Torque	$[N \cdot m]$
V	Volume	$[m^3]$
α	Thermal diffusivity	$[m^2/s]$
α	Volume fraction	[-]
γ	Damping coefficient	[-]
δ	Change in value	[-]
δ	Kronecker delta	[-]
ϵ	Turbulent kinetic dissipation rate	$[m^2/s^3]$
ρ	Density	$[kg/m^3]$
τ	Shear stress	[Pa]
τ_r	Particle relaxation time	[s]
$\bar{\bar{\tau}}$	Stress Tensor	[Pa]
σ	Turbulent Prandtl number	[-]

μ	Dynamic viscosity	$[\mathrm{Pa} \cdot \mathrm{s}]$
μ_t	Turbulent viscosity	$[\mathrm{m}^2/\mathrm{s}]$
$\vec{\omega}$	Angular velocity	$[\mathrm{rad}/\mathrm{s}]$
β	Coefficient of thermal expansion	$[\mathrm{K}^{-1}]$
Γ	Fluctuating dilatation	[-]
Δ	Change in value	[-]
Υ	Mass fraction	[-]
Φ	Energy, velocity, momentum	[-]
$\vec{\Omega}$	Relative angular particle-fluid velocity	$[\mathrm{rad}/\mathrm{s}]$

Contents

1 Introduction

The European Union (EU) has a goal of achieving climate neutrality by 2050[3], while the individual member countries might have developed more ambitious goals to achieve climate neutrality even sooner. Among the more ambitious countries are Denmark, as their climate goals specify climate neutrality by the year 2045 and a 110% reduction by 2050, compared to 1990 levels.[4] The largest contributor to global CO_2 emissions is the power sector with 38.1% of total global emissions in 2023, which is almost double the amount of the second largest contributor (transport 20.7%).[5] Additionally, the largest contributor to CO_2 emissions in the EU is also power production, listed as energy supply, but is only responsible for ≈25% while the transport sector and industry closely follow with an individual emission of ≈20%.[6]

In the power sector the most common type of power plant, for electricity generation, is the pulverized coal (PC) power plant which in 2013 accounted for over 95% of the total global capacity.[7] The first functional PC boiler was introduced in the 1920's, which makes the technology quite mature, but emissions from PC combustion are still difficult to minimize, since it needs to be done in the form of scrubbing and capture. Another technology used for power production is the circulating fluidized bed (CFB) boiler, which is still under development. The CFB boiler could replace the PC boilers as their overall efficiencies (boiler and thermal) are quite similar. Furthermore, the CFB boiler is promising due to the lower emissions which is a consequence of the lower operating temperature, longer residence time and possibility for in situ green house gas (GHG) capture, by for example feeding limestone with the fuel to reduce SO_x levels in the exhaust gasses.[7] Additionally, the CFB boiler offers more flexibility when it comes to fuel type and quality, due to the long residence time, low volatile fuels still undergo complete combustion and the low quality fuels such as coal with a high ash content does not propose a problem in CFB as in PC boilers. This is due to the lower operating temperature resulting in the ash not melting, which otherwise would cause slagging of components.[7] The key differences to note, between PC- and CFB boilers, are the possibility for reduced GHG emissions and the lower operating temperature, reducing the additional system components needed. Although the transition to green energy sources is crucial, power plants fueled by carbon

fuels might remain essential for maintaining grid stability and ensuring security of supply. Therefore it is important to develop newer technologies, like CFB boilers, in order for these to mature and reduce emissions even further.

A combustion process which can be utilized by both PC- and CFB boilers are oxy-combustion where pure oxygen is used for combustion instead of air in order to minimize the formation of nitrid oxides (NOx). Using oxy-combustion ensures that the main product of the reactions consists of H_2O and CO_2, with very little NOx present in the flue gas. By condensing H_2O vapor from the flue gas, CO_2 can be captured from the power plant in a cost-effective manner. As of now the production of pure oxygen is a costly process, but in the future energy visions which include electrolysis where the by-product is pure oxygen, the oxygen should not pose a concern for future energy plants.

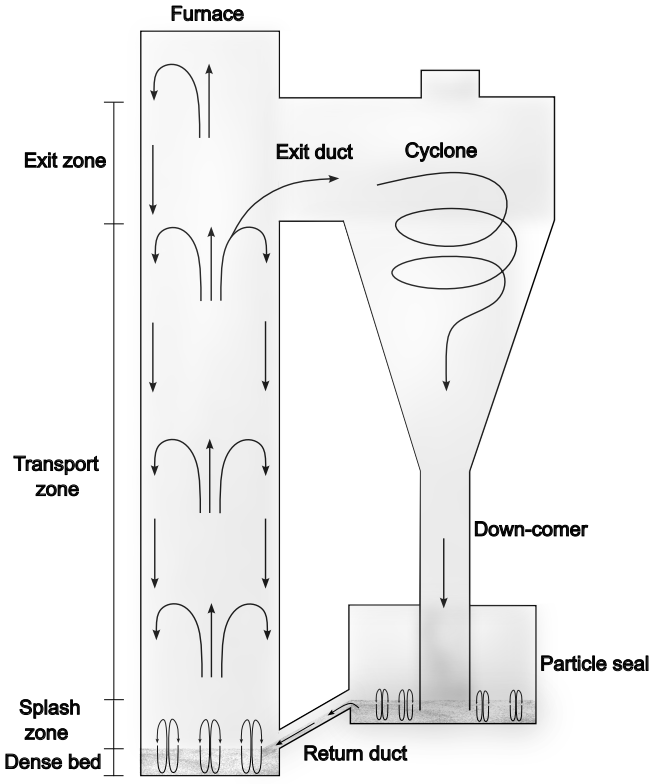

Figure 1.1: Illustration of a CFB boiler inspired by [8]

A CFB boiler is illustrated in Figure 1.1. It is used for generating steam by burning fossil fuels in a furnace that is operated under specific hydrodynamic conditions. Fine solids are

transported through the furnace at a velocity exceeding the terminal velocity of the average particles. However, there is some refluxing of solids to ensure a uniform temperature in the furnace. The furnace holds a large amount of non-combustible solids, that are lifted and accelerated by the high velocity caused by a mixture of combustion and air being blown into the bottom of the furnace. The major fractions of the solids leaving the furnace are captured in a cyclone and recirculated back close to the base of the furnace, at a rate that is able to satisfy the minimum degree of refluxing of solids in the furnace. [8] One advantage that CFB boilers posses, is the fuel flexibility, which is especially attractive in regards to the fluctuating fuel market price. Fuel particles make up less than 3 % of the mass fraction of solids in the CFB, where the rest of the solids consists of non-combustibles like ash, sand and sorbents. The dense bed condition inside the CFB furnace provides a desirable mixing of gas-solid and solid-solid. As a result of this mixing, the fuel particles fed into the furnace are dispersed into the non-combustible solids, where they quickly reach the ignition temperature and combust, without any significant temperature drop in the rest of the non-combustible solids. [8] CFB-boilers also offer the opportunity to implement carbon capture technologies in situ, this is especially true when using oxy-combustion in the CFB boiler.

1.1 Literature study

The development of CFB boiler technology is still ongoing and publications on CFB are plentiful but are dominated by investigations on hydrodynamic behavior ([9], [10], [11], [12], [13], [14], [15], [16], [17], [18]) and the choice and optimization of the model ([19], [20], [21]). The combustion is investigated less in 2D approaches where few publications are found([22], [23]) while publications on 3D modelling are more abundant ([24], [25], [26], [27], [28]). In relation to the reduction of GHG, the combustion process in CFB boilers is of great interest. The publications on combustion have some similarities, such as multiphase modeling and investigation of oxy-combustion, whereas, to the knowledge of the authors, only Wua et al. [26] investigate combustion with and without warm recycled flue gas. Publications on 2D simulations of combustion in CFB boilers are scarce, compared to that of 3D simulations. According to Upadhyay et al. [15] a 3D model predicts the flow hydrodynamics along the reactor height with higher accuracy than a 2D model. In addition, Kun et al. [29] compares a 3D, simplified 3D, and 2D model and concludes that the 2D model overestimates properties such as temperature, particle concentration and particle velocity. Multiple CFD software (Barracuda VR, Ansys FLUENT® and GAMBIT) are used in the literature and most publications using the Ansys FLUENT software are incorporating user-defined functions (UDF) to some degree ([23], [24], [25], [27], [28]).
This project aims to investigate the oxy-fuel combustion in a coal-fired CFB boiler using the available models in the Ansys fluent software. The investigation is focused on the compatibility of the Eulerian-Lagrangian multiphase model in combination with the default species transport combustion model in Ansys fluent, without incorporation of UDFs.

2 Problem Statement

The importance of development and research within the CFB technology have been established. To perform valuable research within the field, it is important to develop models which are valid for simulating different scenarios. Since Ansys FLUENT® is an industry-leading simulation software and widely used within literature, it is relevant to investigate its applicability without the use of UDFs, which can be a time consuming task to develop. This leads to following problem statement

How can combustion combined with the multiphase flow existing in a CFB be modelled and simulated in Ansys Fluent® without the incorporation of UDFs?

Subtasks

- Determine an approximate accuracy of the mesh which is used for simulation.
- Compare the particulate flow distribution using available models for 4-way-coupling.
- Validate the model using available experimental data from literature.

2.1 Delimitations and Assumptions

- The heat and energy output of the CFB boiler is not investigated, and the 100 kW output is only regarded by matching the mass flow of coal to 100 kW.
- UDF's will not be used.
- Only the furnace, cyclone, downcomer and loop seal will be simulated.
- The dynamics of the system will not be investigated.

3 Methodology

The simulations in this project are inspired by the geometry detailed in [2] which is based on the boiler, cyclone, down comer and loop seal from the experimental setup of Li et al. [1], where the experimental data is also obtained from. In this chapter the geometry and relevant information regarding the inlet conditions from [2] and [1] will be presented. This is followed by the computational domain, which includes the mesh constructed for the simulations and important criteria to have in mind when constructing a mesh for CFD simulations. Lastly, the models applied for the simulations, and the settings for these, will be stated, while additional information regarding the modelling, which is not directly related to Ansys Fluent, will be clarified in Chapter 5. The computational resources available for this project consists of an AMD EPYC 7543P processor with 32 cores and 256 GB of DDR4 memory.

3.1 Geometry

The CFB investigated in this is based on the 100 kW oxy-fuel CFB boiler installed at the Institute of Engineering Thermophysics of the Chinese Academy of Sciences. For simplicity, a numerical 3D model is only created of the boiler part of the system, which includes the furnace, cyclone separator, downcomer, and a loop seal. The numerical domain is based on the geometry shown in Figure 3.1 which is a part of the experimental setup that is investigated in [1], where the simplified geometry is described by Gu, Zhong, and Yu [2].

Using a geometry with a closed full loop makes the use of UDF's for recirculation obsolete. The coal inlet is placed right above the reflux connection between the loop seal and the riser at a height of 600 mm, and the secondary air inlet in a height of 1700 mm. The only outlet is located at the top of the cyclone, which feeds the particles to the downcomer. The function of the loop seal is to capture the solids, to make sure they are slowly fed back into the riser. In Table 3.1 dimensions of the different in- and outlets are listed.

Table 3.1

Dimensions of in- and outlets	
Primary air inlet	Ø 100 mm
Secondary air inlet	Ø 40 mm
Loop seal inlet	91 x 280 mm
Coal inlet	Ø 40 mm
Fuel-gas outlet	Ø 40 mm

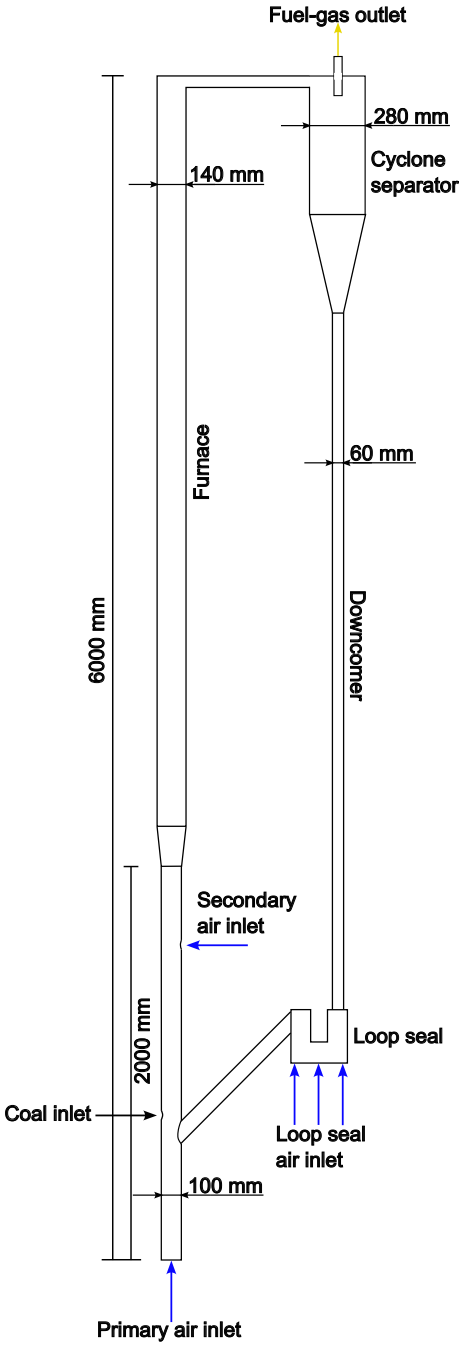

Figure 3.1: A sketch of the 100 kW oxy-fuel CFB boiler which includes dimensions and in- and outlet surfaces. Based on [2]

3.2 Meshing criteria

When creating the computational domain for a geometry,
there are important factors to consider, if you want to ensure a uniform and grid independent solution. A figure showing these criteria can be seen in Figure 3.2.
The **skewness** of a cell depends on the angle between the cell sides. A very small or large angle in the cell surface will result in a skewed cell, this is true for both quadrilateral cells and triangular cells. It is best to keep the skewness < 0.8 and the average below 0.35. A high skewness can affect the interpolation of the cell centered quantities to the face center. It also adds numerical diffusion and wiggles to the solution and affects the convective and diffusive terms. **Aspect ratio** is defined as the ratio between the lengths of the cell sides **a** and **b** ($\frac{\mathbf{a}}{\mathbf{b}}$), and should generally be kept below 5. This is however not the case for the boundary layer, where the aspect ratio can be up to 50. **Growth ratio** is another criterion that is important to remember when creating the computational domain. It is defined by the growth relative to the neighboring cell in the case of the figure below, this would correspond to $\frac{c}{a}$, and it is best to keep this below 1.2 to ensure a smooth transition.

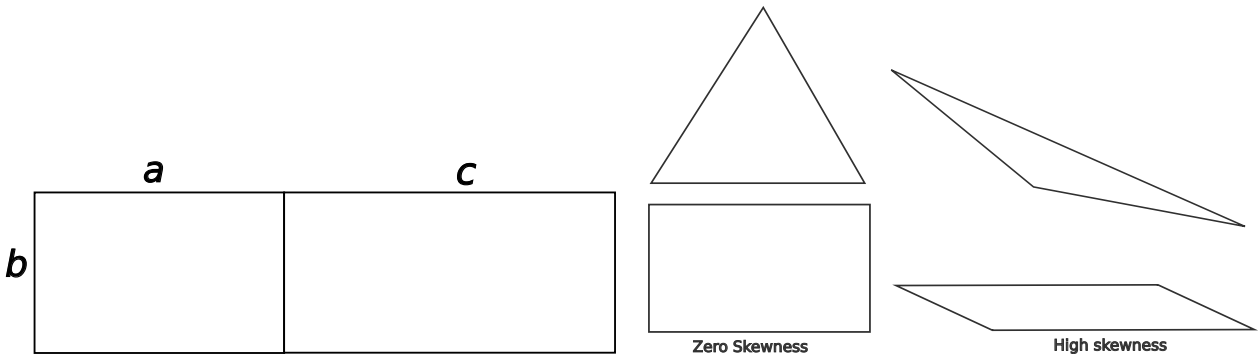

(a) A figure depicting the different sides of a cell, to illustrate apect ratio and growth ratio

(b) A figure to show the skewness of a cell for both a quadrilateral cell and a triangular cell

Figure 3.2: Figures to illustrate skewness, aspect ratio and growth ratio

3.3 Computational Domain

When generating the mesh it is important to consider which cell type to use in order to obtain a good mesh. The cell type that was chosen for this project was the poly-hexcore, a close-up of the generated mesh using these cells can be seen in Figure 3.3.Cells like polyhedrons are effective in filling out the space for the transition layer, which results in a reduction of cells of up to 30 % if poly-hexcore is used compared to hexcore. Hexcore will use tetrahedrons in the transition layer, which will require more cells to occupy the same volume. It is important to notice that the addition of boundary layers increases the amount of cells in the computational domain. In Figure 3.3 a part of the cyclone and the exit duct is depicted.

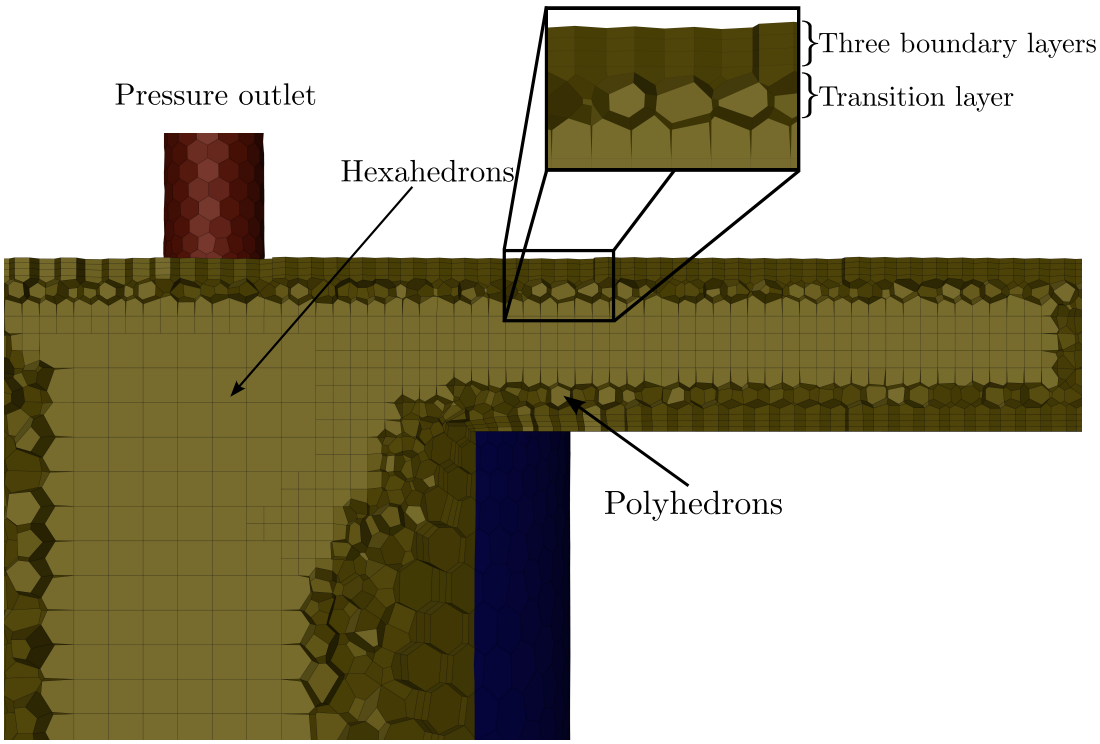

Figure 3.3: Section of a generated mesh containing 284551 cells with 3 boundary layers.

The settings used for the mesh are found in Table 3.2, some of these settings were the default settings in FLUENT® meshing software, while local sizing was added to each individual section.

Table 3.2: The settings used for all mesh containing boundary layers

Settings in FLUENT® meshing software	
Volume mesh	Poly-hexcore
Buffer layers	2
Peel layers	1
Boundary layers	3
Transition ratio	0.272
Growth ratio	1.2
Off-set method	Smooth transition
Min/max aspect ratio	1-10

3.4 Models and Settings

The models and settings used for the simulations will be mentioned shortly while the theory behind the models will be described in depth in Chapter 4. The solver is chosen to be the transient pressure-based with velocity formulation on absolute, and gravity enabled. The models enabled from the model menu tab in FLUENT® are as follows:

- Multiphase - Hybrid Eulerian-Lagrangian, DDPM with one continuous phase and two discrete phases.
- Discrete Phase model with injections.
- Energy.
- Species - Species transport with reactions.
- Viscous - Realizable k-epsilon, standard wall function - Dispersed.

These are the models enabled for the final simulation, while the combination of models might vary from simulation to simulation, it will be stated in Chapter 6 which models are enabled for the resulting simulation(s).

3.4.1 Gas-Solid Flow

In order to simulate the gas-solid flow in the CFB the hybrid Eulerian-Lagrangian model in FLUENT® is used, which is the dense discrete phase model (DDPM).
For the DDPM model the default settings for phase interaction are retained, while the option "volume fraction approaching continuous flow limit" are disabled and the "granular" option enabled for the particulate phases. The settings in the phase interactions tab are stated in Table 3.3.

Table 3.3: DDPM phase interaction settings.

Forces	
Drag Coefficient:	averaged-discrete-phase-drag
Modification:	none
Lift Coefficient:	dpm-averaged
Wall Lubrication:	dpm-averaged
Surface Tension Coefficient:	none
Interfacial Area	
Interfacial Area:	ia-particle

Additionally, the discrete phase model (DPM) is enabled for injection of particles. The injection are performed using the file injection option in the injection window. Injection files are generated using MATLAB, each line in a text file corresponds to a particle parcel, which can include any number of particles, and the injection files should have the following format:

$$((x, y, z, u, v, w, D, T, \dot{m})injection\#) \tag{3.1}$$

The script used to generate the particle injection file for the riser can be seen in Appendix A.1. The settings for the DPM is shown in table Table 3.4

Table 3.4: DPM settings.

Particle Treatment	
Unsteady Particle Tracking	on
Inject Particles at:	Fluid Flow Time Step
Tracking	
Max. Number of Steps:	1500
Step Length Factor:	5
High-Res Tracking:	off
Physical Models	
Virtual Mass Force:	on
Pressure Gradient Force:	on
Numerics	
Accuracy Control:	off
Parallel	
Methods:	Hybrid

Additionally, the drag model used in the injection properties window is set to Wen-Yu.

3.4.2 Combustion settings

The ultimate and proximate analysis *as received* (AR), together with the properties of the coal, can be found in Table 4.2. These are the default values given for the material "Coal_lv" in Fluent and corresponds to the ultimate and proximate analyses used by Gu, Zhong, and Yu [2].

Table 3.5: Analysis and properties of coal used in the combustion reaction

	C	**H**	**O**	**N**	**S**
Ultimate analysis [$wt\%$]	58.08%	3.73%	8.58%	1.04%	0.32%
	Volatiles	**Fixed carbon**	**Ash**	**Moisture**	
Proximate analysis [$wt\%$]	27.37%	44.38%	26.05%	2.2%	
	LHV	**Dry density**	**Volatile molecular weight**	**Fraction of N in char**	
Coal properties	$24 \cdot 10^6$ [J/kg]	1400 [kg/m^3]	30 [kg/kmol]	0.7	

Species model

The species model chosen is the species transport, with further information in Table 3.6 below. Additionally, the models used for the devolatilization and combustion of the combustible particle is stated.

Table 3.6: Species model settings.

Species transport	
Reactions:	Volumetric
Options:	Diffusion Energy Source
Turbulence-Chemistry Interaction (TCI):	Finite-Rate/Eddy-Dissipation
Phase Material:	coal-lv-volatiles-air
Chemistry Solver:	None - Direct Source
Combusting particle - coal-lv	
Devolatilization Model:	single-rate
Combustion Model:	diffusion-limited

3.4.3 Schemes

The differencing schemes applied for the simulations can be seen in Table 3.7, the first order schemes were deemed fitting and a clarification on this choice is given in Section 4.5.

Table 3.7: Schemes used for the simulation.

Spatial Discretisation	
Gradient:	Green-Gauss Node Based
Pressure:	PRESTO!
Momentum:	First Order Upwind
Volume Fraction:	First Order Upwind
Turbulent kinetic energy and dissipation rate:	First Order Upwind
Energy:	First Order Upwind
Species:	First Order Upwind

3.4.4 Summary

In Table 3.8 the applied models in the final simulation with combustion is summarized and the accompanying important settings.

Table 3.8: Models activated and the accompanying settings.

Dense Discrete Phase Model					
Drag Coefficient:	Lift Coefficient:	Wall Lubrication:	Surface Tension:	Interfacial Area:	-
averaged-discrete--phase-drag	dpm-averaged	dpm-averaged	none	ia-particle	-
Discrete Phase Model					
Particle Treatment:	Tracking:	Physical Models:	Numerics:	Parallel:	-
Unsteady Tracking	Max. Steps: 1500	Virtual Mass and Pressure Gradient Force	Accuracy Control: off	Hybrid	-
Species Model					
Reactions:	Options:	TCI:	Phase Material:	Chemistry Solver	Combusting particle models:
Volumetric	Diffusion Energy Source	Finite-Rate/ Eddy-Dissipation	coal-lv-volatiles-air	None - Direct Source	single-rate & diffusion-limited
Solution Methods					
Pressure-Velocity Coupling:	Gradient:	Pressure:	Momentum, Volume--Fraction, Turbulence, Energy and Species:	Transient Formulation:	Warped-Face Gradient correction:
Phase Coupled SIMPLE	PRESTO!	Green-Gauss Node Based	First Order Upwind	on	Implicit

4 Theory

Since the software used is FLUENT®, the theory chapter will be based on the theory behind the software as described by Ansys in their theory guide ([30]), unless otherwise stated. In FLUENT® the conservation equations for mass and momentum are solved for all flows, while additional equations are solved when models like energy, turbulence and combustion are enabled. The governing equations are covered in the following section followed by the additional models applied and the corresponding equations solved in the simulation.

4.1 Governing Equations

The transport equation on standard form in [31] is given as:

$$\underbrace{\frac{\partial(\rho\phi)}{\partial t}}_{\text{I}} + \underbrace{div(\rho\phi\mathbf{u})}_{\text{II}} = \underbrace{div(\Gamma\phi)}_{\text{III}} + \underbrace{S_\phi}_{\text{IV}} \tag{4.1}$$

the terms are described as: (I) Rate of increase of ϕ in fluid element, (II) Net rate of flow of ϕ out of fluid element, (III) Rate of increase of ϕ due to diffusion and (IV) Rate of increase of ϕ due to sources. In the finite volume method (FVM) all terms in the transport equation are integrated over a control volume.[31, p. 25] Each momentum equation must satisfy the continuity equation:

$$\frac{\partial}{\partial x}(\rho\mathbf{u}) + \frac{\partial}{\partial y}(\rho\mathbf{v}) + \frac{\partial}{\partial z}(\rho\mathbf{w}) = 0 \tag{4.2}$$

4.2 Gas-Solid Flow

The Eulerian-Lagrangian multiphase model in FLUENT® is able to process multiple separate interacting phases. These phases can be liquids, gases, or solids in almost every combination. A Eulerian treatment is used for each fluid or gas phase while a solid phase is defined as a discrete phase and is calculated using a Lagrangian approach.

The mass and momentum conservation are, in Ansys, on the following form:

$$\frac{\partial \rho}{\partial t} + \nabla(\rho \vec{v}) = S_{DPM} + S_{other} \tag{4.3}$$

$$\frac{\partial \rho \vec{v}}{\partial t} + \nabla(\rho \vec{v}\vec{v}) = -\nabla p + \nabla \tau + \rho \vec{g} + \vec{F}_{DPM} + \vec{F}_{other} \tag{4.4}$$

A limitation of the Lagrangian multiphase model is that it does not take into account the volume fraction of the particulate phase. To overcome this limitation, Equation 4.3 and 4.4 can be extended to following form for an individual phase p:

$$\frac{\partial}{\partial t}(\alpha_p \rho_p) + \nabla(\alpha_p \rho_p \vec{v}_p) = \sum_{q=1}^{nphases} (\dot{m}_{qp} - \dot{m}_{pq}) \tag{4.5}$$

$$\begin{aligned} \frac{\partial}{\partial t}(\alpha_p \rho_p \vec{v}_p) + \nabla(\alpha_p \rho_p \vec{v}_p \vec{v}_p) = & -\alpha_p \nabla p + \nabla \left[\alpha_p \mu_p \left(\nabla \vec{v}_p + \nabla \vec{v}_p^T \right) \right] + \alpha_p \rho_p \vec{g} \\ & + F_{vm,lift,user} + \sum_{q=1}^{nphases} \left(\vec{K}_{qp} \left(\vec{v}_q - \vec{v}_p \right) + \dot{m}_{pq} \vec{v}_{pq} - \dot{m}_{qp} \vec{v}_{qp} \right) \\ & + K_{DPM} \left(\vec{v}_{DPM} - \vec{v}_p \right) + S_{DPM,explicit} \end{aligned} \tag{4.6}$$

The momentum exchange terms are split into an explicit part and an implicit part, these momentum exchange terms are denoted by DPM, where v_{DPM} is the particle averaged velocity and K_{DPM} represents the particle averaged interphase momentum exchange coefficient. To limit the accumulation of particles a special treatment of the particle momentum equation (Eq. 4.6) is applied when it exceeds a user specified limit for the volume fraction. When defining discrete phases using the DDPM in FLUENT®, it is necessary to define injections for the discrete phase using the DPM.

4.2.1 Discrete Phase Model

Particles in FLUENT® are tracked by integrating the force balance on the particle, which is written in a Lagrangian reference frame. The force balance equates the particle inertia with the forces acting on the particle:

$$m_p \frac{d\vec{u}_p}{dt} = m_p \frac{\vec{u} - \vec{u}_p}{\tau_r} + m_p \frac{\vec{g}(\rho_p - \rho)}{\rho_p} + \vec{F}_{other} \tag{4.7}$$

Where m_p is the particle mass $\vec{u}_p$ is the particle velocity ρ is the fluid density and ρ_p is the density of the particle. $\vec{F}_{other}$ is simply additional forces, $m_p \frac{\vec{u}-\vec{u}_p}{\tau_r}$ is the drag force and τ_r is the particle relaxation time, which can be calculated by

$$\tau_r = \frac{\rho_p d_p^2}{18\mu} \frac{24}{C_d \mathrm{Re}} \tag{4.8}$$

Where μ is the molecular viscosity, d_p is the particle diameter and Re is the relative Reynolds number which is calculated as

$$\mathrm{Re} = \frac{\rho d_p |\vec{u}_p - \vec{u}|}{\mu} \tag{4.9}$$

Additionally, the DPM takes into account the particle rotation through a particle torque balance. The torque balance is solved by an extra ordinary differential equation for the particles angular momentum:

$$I_p \frac{d\vec{\omega}_p}{dt} = \frac{\rho_f}{2} \left(\frac{d_p}{2}\right)^5 C_\omega |\vec{\Omega}| \cdot \vec{\Omega} = \vec{T} \tag{4.10}$$

where I is the momentum of inertia, $\vec{\omega}$ is the angular velocity, C is the rotational drag coefficient, $\vec{T}$ is the torque applied to a particle in the fluid domain and $\vec{\Omega}$, the relative angular particle-fluid velocity, is defined as:

$$\vec{\Omega} = \frac{1}{2} \nabla \times \vec{u}_f - \vec{\omega}_p \tag{4.11}$$

where in both Equation 4.10 and 4.11 the subscripts p and f denotes particle and fluid respectively. Furthermore, for a spherical particle the momentum of inertia is calculated by

$$I_p = \frac{\pi}{60} \rho_p d_p^5 \tag{4.12}$$

When enabling the 'granular' option in the DDPM, the particle interaction is computed

from the stress tensor given in the Kinetic Theory of Granular Flows (KTGF) by:

$$\vec{F}_{interaction} = -m_p \frac{1}{\rho_p} \nabla \overline{\overline{\tau}_s} \tag{4.13}$$

with the particle interaction in Equation 4.13 added to the right hand side of Equation 4.7. Included in the DPM capabilities of FLUENT® is the physical model Discrete Element Method (DEM), which is typically used in simulations containing a high volume fraction of particles where particle-particle interactions are important. The DEM model is, compared to the KTGF approach in the DDPM, computationally expensive while the KTGF approach is computational efficient. The DEM model is based on soft sphere collision.

Discrete Element Method

The DEM allows for particle collisions to be calculated with fairly high accuracy. It is suitable when simulating granular matter such as coal, gravel or sand and in general where the particle loading is high. The DEM implementation accounts for the resulting forces from particle collisions, these forces are calculated in the DPM approach through the F_{other} term in Equation 4.7. The forces are determined by the overlap between spheres or spheres and a boundary, also referred to as the deformation of the sphere. [30]
The collision force law applied in the simulations performed in this project is the spring-dashpot. The spring constant can be estimated:

$$k = \frac{\pi v^2}{3\varepsilon_D^2} D\rho \tag{4.14}$$

where v is the relative velocity between the two colliding particles and ε is the allowable overlap defined as a fraction of the diameter. The force on particle one can be calculated by:

$$\vec{F}_1 = k\delta\vec{e}_{12} \tag{4.15}$$

where e_{12} is a defined as a unit vector from particle one to particle two as:

$$\vec{e}_{12} = \frac{(x_2 - x_1)}{||x_2 - x_1||} \tag{4.16}$$

here x represents a position. When extending the spring force law to the spring-dashpot a coefficient of restitution is also defined along with some extended expression for the force resulting in

$$\vec{F}_1 = (k\delta + \gamma(\vec{v}_{12} \cdot \vec{e}_{12}))\vec{e}_{12} \tag{4.17}$$

which includes a damping coefficient γ with the condition $\gamma \geq 0$ and the relative velocity $\vec{v}_{12}$. An illustration of the overlap/deformation taken into account in the DEM collision approach can be seen in Figure Figure 4.1

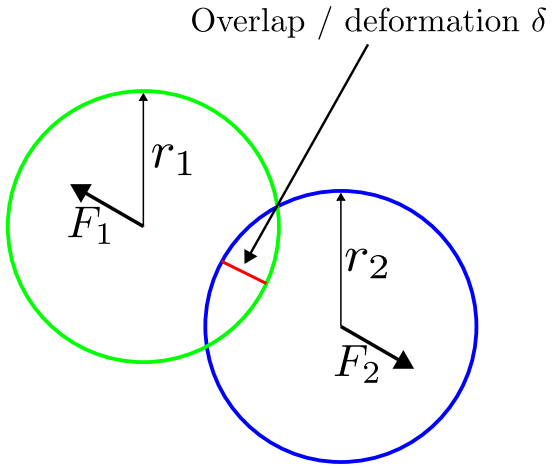

Figure 4.1: Illustration of the deformation of particles used for calculation in the DEM approach. Based on Figure 12.27 from [30, p. 577]

4.3 Turbulence Modelling

The most common turbulence models used in CFD is based on the Reynolds-Averaged Navier-Stokes (RANS) equations. It is the most widespread simulation approach and is based upon averaging the Navier-Stokes equations to obtain equations describing the mean of the fluid flow. The result is similar to the original Navier-Stokes equations but includes additional terms in the momentum equations to describe the Reynolds stresses. The idea of averaging the "unsteadiness" of the flow throughout the domain is visualized in Figure 4.2.[31][32]

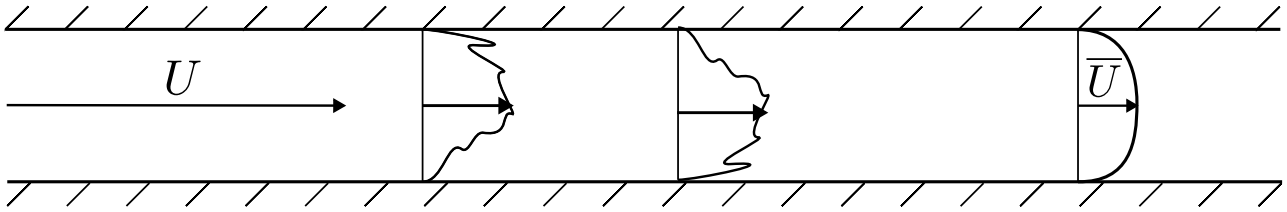

Figure 4.2: Visualization of the averaging of the flow field performed in RANS simulations.

The RANS equations for continuity and momentum are written in tensor form in Eq. 4.18 and 4.19 respectively.[31, p.63-64]

$$\frac{\partial U_i}{\partial x_i} = 0 \tag{4.18}$$

$$\rho\left(\frac{\partial \mathrm{U}_i}{\partial t} + \frac{\partial \mathrm{U}_i \mathrm{U}_j}{\partial x_j}\right) = -\frac{\partial p}{\partial x_i} + \mu\frac{\partial \mathrm{U}_i}{\partial x_j x_j} + \frac{\partial}{\partial x_j}\left(-\rho\overline{u_i' u_j'}\right) \tag{4.19}$$

The last term on the right hand side of Equation 4.19 is the turbulent or Reynolds Stress

$$-\rho\overline{u_i' u_j'} = \mu_t\left(\frac{\partial U_i}{\partial x_j} + \frac{\partial U_j}{\partial x_i}\right) \tag{4.20}$$

A more general expression includes the following term on the right hand side of Equation 4.20

$$-\frac{2}{3}\rho k\delta_{ij} \tag{4.21}$$

it ensures correct results for the normal Reynolds stress, but is normally dropped in textbooks for simplicity. Here k is the turbulent kinetic energy per unit mass and δ is the Kronecker delta defined by following conditions:

$$\delta_{ij} = 1 \quad if \quad i = j \qquad and \qquad \delta_{ij} = 0 \quad if \quad i \neq j \tag{4.22}$$

The most commonly used turbulence model in the literature on CFB is the realizable k-ϵ model. It is a two-equation turbulence model, which means it determines both the turbulent length and time scale by solving two separate transport equations.[30, p.49] The transport equation concerning the turbulence kinetic energy k is:

$$\frac{\partial}{\partial t}(\rho k) + \frac{\partial}{\partial x_i}(\rho k u_i) = \frac{\partial}{\partial x_j}\left[\left(\mu + \frac{\mu_t}{\sigma_k}\right)\frac{\partial k}{\partial x_j}\right] + G_k + G_b + \rho\varepsilon - Y_M + S_k \tag{4.23}$$

and its rate of dissipation ε is obtained from following transport equation:

$$\frac{\partial}{\partial t}(\rho\varepsilon) + \frac{\partial}{\partial x_i}(\rho\varepsilon u_i) = \frac{\partial}{\partial x_j}\left[\left(\mu + \frac{\mu_t}{\sigma_\varepsilon}\right)\frac{\partial \varepsilon}{\partial x_j}\right] + \rho C_1 S_\varepsilon \tag{4.24}$$
$$- \rho C_2 \frac{\varepsilon^2}{k + \sqrt{v\varepsilon}} + C_{1\varepsilon}\frac{\varepsilon}{k} C_{3\epsilon} G_b + S_\varepsilon$$

where, in both Equation 4.23 and 4.24, G is the generation of turbulence kinetic energy, Y represents the contribution of fluctuating dilatation, C, excluding C_1, are constants, σ is the turbulent Prandtl number and S is an additional source term which can be defined by the user. The value of C_1 is determined by

$$C_1 = max\left[0.43, \frac{\eta}{\eta + 5}\right], \quad \eta = S\frac{k}{\varepsilon}, \quad S = \sqrt{2D_{ij}Sij} \tag{4.25}$$

The main difference between the standard k-ε and realizable k-ε is the formulation of the turbulent viscosity and a modified transport equation for the dissipation rate. Additionally, the realizable k-ε model, in contrary to other k-ε models, does not have a singularity in k in the destruction term of the ε transport equation (third term on the right hand side).[30, p.55] In the study of the full loop CFB based on 3D simulations [2], which is also used for validation, the Large Eddy Simulation (LES) turbulence model is used. The RANS based k-ε turbulence model assumes universal behaviour of all eddies and they are described by a single turbulence model. Since the behaviour of large eddies are highly dependent on the geometry, boundary conditions and body forces, it complicates the search for a widely applicable model. Additionally, the smaller eddies generally have uniform behaviour and are easier to capture with a compact model. The essence of the LES approach is to compute the larger eddies with a time-dependent simulation while the smaller eddies are solved universally, but instead of a time-averaging approach the LES model uses a spatial filtering operation to separate the larger and smaller eddies. [30]

4.4 The energy equation

The energy equation used in the FLUENT® software takes the following form.

$$\frac{\partial}{\partial t}\left(\rho\left(e+\frac{v^2}{2}\right)\right)+\nabla\cdot\left(\rho\vec{v}\left(h+\frac{v^2}{2}\right)\right)=\nabla\cdot\left(k_{eff}\nabla T-\sum_j h_j\vec{J}_j+\vec{\tau}_{eff}\cdot\vec{v}\right)+S_h \quad (4.26)$$

Where k_{eff} is the effective conductivity $(k+k_t)$ and k_t is the turbulent thermal conductivity, this is defined according to the turbulence model used. $\vec{J}_j$ is the diffusion flux of the species j. The first three terms on the right-hand side of the equation represent energy transfer due to conduction, species diffusion, and viscous dissipation. The last term S_h represents a volumetric heat source that can be pre-defined together with the heat generation rate from the chemical reactions. [30]
The enthalpy h is defined for ideal gases as

$$h=\sum_j Y_j h_j \quad (4.27)$$

Where Y_j is the mass fraction of species j and h_j is the sensible heat of species j, which is the part of the enthalpy that includes only changes in enthalpy due to specific heat.
Furthermore, in multiphase flow theory in FLUENT® concerning energy transfer, the enthalpy equation for the p^{th} phase is solved by:

$$\frac{\partial}{\partial t}\left(\alpha_p\rho_p\left(e_p+\frac{\vec{v}_p^2}{2}\right)\right)+\nabla\cdot\left(\alpha_p\rho_p\vec{v}_p\left(h_p+\frac{\vec{v}_p^2}{2}\right)\right)=H_{conv}+H_{diff}+H_{visc} \quad (4.28)$$
$$+H_{user}+p\frac{\partial\alpha_p}{\partial t}+\sum_{q=1}^{nphases}\left(Q_{qp}+\dot{m}_{pq}h_{pq}-\dot{m}_{qp}h_{qp}\right)+Q_{DPM}+S_{DPM,explicit}$$

where the same denotation as for the particle momentum equation is applied, in which the implicit part Q_{DPM} is defined as:

$$Q_{DPM}=h_{DPM}A_i(T_{DPM}-T_p) \quad (4.29)$$

here A_i is the interfacial area and T_{DPM} is the particle averaged temperature of the discrete phase in consideration.

4.5 Discretisation Schemes

When considering which schemes to choose for a simulation, the most important parameters to consider are conservativeness, boundedness, and transportiveness. In order to ensure conservation of property ϕ for the domain, conservativeness involves guaranteeing the same flux through common surfaces which must be represented in a consistent manner. Additionally, boundedness is used to ensure that the properties in a node are not able to reach values higher or lower than adjacent nodes and is defined as "*... in the absence of sources the internal nodal values of property ϕ should be bounded by its boundary values.*"[31, p. 143], while all coefficients in the discretised equations should have the same sign. Lastly, transportiveness is usually described by the nondimensional cell Peclet number as a measure of relative strengths of convection and diffusion.

$$Pe = \frac{F}{D} = \frac{\rho u}{\Gamma/\delta x} \tag{4.30}$$

where a value of zero corresponds to pure diffusion and a value approaching infinity corresponds to pure convection. In the case of pure diffusion the fluid is stagnant and in the case of pure convection the fluid is completely "stretched" out in the flow direction.[31] Generally, schemes are often referred to based on their order of accuracy. The higher order the scheme the more precise it is, and it therefore provides results with less error. The first order differencing schemes provides stability and are easily implemented while providing a smooth solution. But due to them being highly diffusive for problems with high Reynolds or Peclet numbers, the solution is prone to relatively large deviation from the correct solution. While second order schemes are more precise, the use of these can often lead to an oscillatory solution, and second order schemes are therefore less stable. For stability and convergence reasons the first order differencing schemes are chosen for the simulations in this project. The differencing schemes are based upon finite volume discretisation.[31]
Finite volume discretisation is done by dividing the domain into discrete volumes and each

volume having a representative value at its center, for a one-dimensional domain the cells are numbered 1 to N while in a three-dimensional domain its numbered (i,j,k). A one-dimensional domain is shown in Figure 4.3. For convenience the compass notation is used to describe neighbouring cells and faces, where in the x-direction cells are labelled capital E and W and faces are labelled with lower case e and w (for east and west). Similarly in the y-direction cells and faces are labelled N, S, n and s (for north and south) respectively.

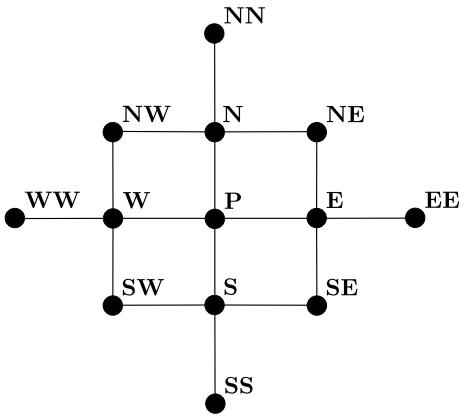

Figure 4.3: General discretisation of a computational domain from cell center P. Inspired by [31]

4.5.1 Upwind Differencing Scheme

The upwind differencing scheme is used for momentum and in contrary to the central differencing scheme, the upwind differencing or also known as "donor cell" differencing takes into account the direction of the flow, for one dimensional flow, by according to [31] setting:

$$\phi_w = \phi_W \quad and \quad \phi_e = \phi_P \tag{4.31}$$

Applying the definitions given in Equation 4.31, the discretised equation, for flow in the positive direction, final form becomes:

$$[(D_w + F_w) + D_e + (F_e - F_w)]\phi_P = (D_w + F_w)\phi_W + D_e\phi_E \tag{4.32}$$

Similarly for the negative flow direction:

$$\phi_w = \phi_P \quad and \quad \phi_e = \phi_E \tag{4.33}$$

Resulting in the following discretised equation:

$$[D_w + (D_e - F_e) + (F_e - F_w)]\phi_P = D_w\phi_W + (D_e - F_e)\phi_E \tag{4.34}$$

Where F and D are defined as the convective mass flux per unit area and diffusion conductance respectively:

$$F = \rho u \quad and \quad D = \frac{\Gamma}{\delta x} \tag{4.35}$$

4.6 Boundary Conditions

In addition to the models, it is important to define the boundary conditions at each boundary. Generally, the boundaries existing in a computational domain are inlet(s), outlet(s) and walls. Furthermore, when defining the boundary conditions using the DPM in FLUENT®, it is necessary to determine the fate of the particles that come into contact with a boundary. The boundary condition for the discrete phases are defined as *reflect* on all boundaries except for the outlet where *escape* is used as the boundary condition.

Inlet

The velocity inlet boundary condition is used to define the flow velocity and other scalar properties that are relevant for the flow at the inlet. The total pressure is not fixed but will increase in response to the computed static pressure to the necessary value which provides the velocity distribution. A velocity magnitude and direction has to be predefined.

Wall

The wall boundary condition is used to bind the fluid and solid region. Using viscous flow, the no-slip boundary condition is enforced at the wall by default. It is possible to specify a tangential velocity component in terms of the translational or rotational motion. Slip can be modelled on the wall by specifying shear.

Outlet

Pressure outlet boundary condition is often chosen in combination with velocity inlet boundary condition. This is because it is not possible to define a velocity inlet while also defining a velocity outlet, since the velocity at the outlet is determined by the development of the flow through the geometry making it impossible to pre-define. The pressure outlet boundary condition requires a specification of a static pressure at the outlet boundary, which is only valid while the flow is subsonic, in case of supersonic flow, the specified pressure will no longer be used.

4.7 Combustion Mechanisms

When modelling combustion in FLUENT®, it is important to consider the mechanism involved in the combustion reaction. This can be taken into account by using the species transport and either finite rate chemistry or Eddy-dissipation. This section will cover the combustion mechanisms involved in the reactions of coal combustion.

4.7.1 Devolatilization of Coal

When coal particles are heated to temperatures higher than 700-1000 K they devolatize, where a portion of the coal is turned into solid residue as char, and the rest is turned into volatiles. After this process, a homogenous reaction for the volatiles and a heterogeneous reaction of the char take place. When coal is the only fuel in the system it can be modelled by two mixture fractions, where one stream represents the char and the other stream represents volatiles. This process is illustrated in figure Figure 4.4.

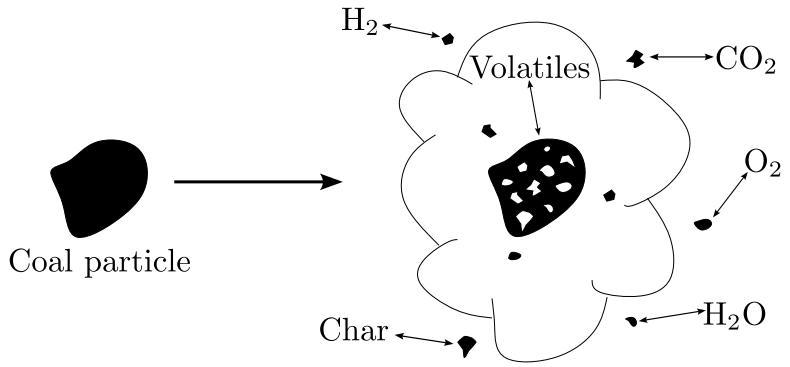

Figure 4.4: Illustration of devolatilization and gasification of coal. Inspired by Lee, Choi, and Kim [33]

There are different coal types that can be chosen in FLUENT® with different default values. Some of these are listed in table Table 4.1 below

Table 4.1: Coal types in FLUENT® with default properties

Coal	Properties			
			Component fraction[%]	
	Density[kg/m^3]	Cp [J/kgK]	Fixed carbon	Volatile matter
Anthracite	1550	1680	85.1	6.9
Coal-lv	1400	1680	79.1	12.9
Coal-mv	1400	1680	64.4	27.6
Coal-hv	1400	1680	57.5	34.5

The default reaction in FLUENT® when choosing species transport and Eddy Dissipation is the oxidation of char.

$$C(s) + O_2 \longrightarrow CO_2 \tag{4.36}$$

FLUENT® provides several models for species transport and several reactions to model the gas phase reacting flows. Volatiles tend to burn very quickly as they enter the computational domain, which would be controlled by the chemical reaction rates. The combustion reaction of the volatiles in FLUENT® is shown in Table 4.2. [33]

Table 4.2: Analysis and properties of coal used in the combustion reaction, as analysed in [33].

Volatiles of coal types	Cp_{vol} [J/kgK]	M_{vol} [g/mol]	Combustion reactions
Anthracite	1500	13.21	anthracite$_{vol}$ + 2.2070O_2 → 0.1CO_2 + 4.408H_2O
Coal-lv	1500	23.82	Coal-lv$_{vol}$ + 2.979O_2 → CO_2 + 4.17H_2O
Coal-mv	1500	17.237	Coal-mv$_{vol}$ + 1.706O_2 → CO_2 + 1.543H_2O
Coal-hv	1500	18.412	Coal-hv$_{vol}$ + 1.598O_2 → CO_2 + 1.417H_2O

4.7.2 Species Transport

There are several ways of modelling combustion reactions in FLUENT®. One way to do so is to use species transport and finite-rate chemistry. Using this approach, the mixing and transport of the chemical species is solved using conservation equations that describe the convection, diffusion and reaction sources for each species. It is possible to calculate multiple simultaneous chemical reactions, with reactions occurring in the fluid phase and on wall or particle surfaces. When the conservation equations are solved for the chemical species, FLUENT® predicts the local mass fraction of each species Y_i through the solution of a convection-diffusion equation for the i^{th} species. The equation is expressed as

$$\frac{\partial}{\partial t}(\rho Y_i) + \nabla(\rho \vec{v} Y_i) = -\nabla \vec{J}_i + R_i + S_i \tag{4.37}$$

Where ρ is the mixture density, $\vec{v}$ is the velocity of the diffusing species, R_i is the net rate of production of species i by chemical reaction. S_i is the rate of production by adding the dispersed phase plus any user-defined sources.[30] The treatment of the species transport in the energy equation for multi component mixing flows is described by defining the transport of enthalpy due to species diffusion:

$$\nabla \cdot \left[\sum_{i=1}^{n} h_i \vec{J}_i \right] \tag{4.38}$$

here J is the mass diffusion of species i. This enthalpy due to species diffusion is important to consider, as it can significantly affect the enthalpy field. Especially in scenarios where the species Lewis number defined by

$$Le_i = \frac{k}{\rho C_p D_{i,m}} \tag{4.39}$$

is far from unity. Where k is the thermal conductivity, C_p is the specific heat and $D_{i,m}$ is the mixture averaged diffusion coefficient. The Lewis number can also be expressed in terms of the Prandtl number (Pr) and the Schmidt number (Sc):

$$Le = \frac{Sc}{Pr} \tag{4.40}$$

4.7.3 Finite-Rate Chemistry

The devolatilization model is applied to a combusting particle when the particle reaches the vaporization temperature and remains in effect while the mass of the particle exceeds the mass of the non-volatiles in the particle. The composition of the volatiles is represented as $C_XH_YO_Z$. [33]

FLUENT® is able to use three different models to describe the devolitalization using finite rate chemistry; the single kinetic rate model, the constant rate model and the two competing rate model. When kinetics are investigated a rate constant k is calculated to describe the reaction rate of the specific reaction. The single rate is determined using the Arrhenius equation:

$$k = A \cdot \exp\left(\frac{-E}{RT}\right) \tag{4.41}$$

Where k is the reaction rate in [mol/s], A is the pre-exponential factor and E is the activation energy in [kJ/mol].

The two competing model considers the fact that volatile yields at high temperatures has been observed to be substantially higher compared to the proximate volatile content, and can be derived from the Arrhenius equation:

$$k_1 = B_1 \cdot \exp\left(\frac{-E_1}{RT}\right) \tag{4.42}$$

$$k_2 = B_2 \cdot \exp\left(\frac{-E_2}{RT}\right) \tag{4.43}$$

Where B_1 and B_2 are considered pseudo pre-exponential factors and E_1 and E_2 are pseudo activation energies.

The different types of coal listed in Table 4.1 all have different values for each constant in this equation, and in the scope of this project the type of coal that was used was coal-lv, with corresponding values of $A = 3.82\text{e}{+05}$ and $E = 74\text{e}{+06}$.[33]

4.7.4 The Eddy Dissipation Model

In some conditions the overall rate of reaction for the combustion is controlled by turbulent mixing. For very high temperatures and non-premixed flames, the turbulence slowly convects and mixes the fuel and oxidizer into reaction zones where they burn quickly. The eddy-dissipation model takes this mixing into account.[30] The net rate of production of species i due to the reaction R_i is given by the smaller of the two expressions below;

$$R_{i,r} = (v''_{i,r} - v_{i,r}) M_{w,i} A \rho \frac{\varepsilon}{k} \min_{\mathcal{R}} \left(\frac{Y_{\mathcal{R}}}{v'_{\mathcal{R},r} M_{w,\mathcal{R}}} \right) \tag{4.44}$$

$$R_{i,r} = (v''_{i,r} - v_{i,r}) M_{w,i} A B \rho \frac{\varepsilon}{k} \left(\frac{\sum_P Y_P}{\sum_J^N v''_{j,r} M_{w,j}} \right) \tag{4.45}$$

Where R is the net rate of production of each species i, v' and v'' are stoichiometric coefficients, A and B are empirical constants where $A = 4.0$ and $B = 0.5$. The correlation $\frac{\varepsilon}{k}$ is the large-eddy mixing time scale and Y_p is the mass fraction of product species, and $Y_{\mathcal{R}}$ is the mass fraction of reactant species seen in 4.45. [30]

4.7.5 Finite-rate/Eddy-Dissipation

FLUENT® also offers a combination of Finite-rate and Eddy-dissipation. In this combination of models it is assumed that reactions are fast and that the system is only mixing limited, and when that is not the case, it is combined with Finite-Rate. This will enable the kinetic rate to be calculated in addition to the reaction rate predicted by the eddy-dissipation model. Then the slowest reaction rate is used, if turbulence is slow and mixing is slow the reaction rate is limited by the eddy dissipation model. When turbulence is high but the kinetic rate is slow the reaction rate is limited by the kinetics.

4.8 Pressure-Based Solvers

The pressure-based solver implemented in FLUENT® uses an algorithm which can be classified in a subcategory of methods called the projection method. In this method, the imperative of mass conservation (continuity) within the velocity field is achieved by addressing a pressure (or pressure correction) equation. This equation is formulated through a derivation from both the continuity and momentum equations, ensuring that the corrected velocity field satisfies continuity. The governing equations are non-linear and all coupled to one another, which requires the solution method to be iterative, such that the entire set of governing equations is solved repeatedly until the solution converges. [30]

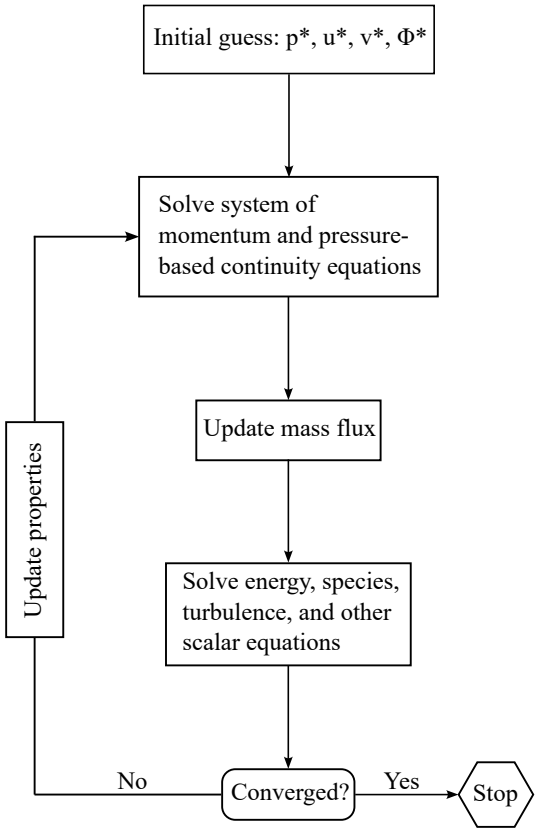

Figure 4.5: A flowchart depicting the steps in the pressure-based coupled solver algorithm [30, p. 957]

There are two pressure-based solvers available in FLUENT®, a **segregated algorithm** and a **coupled algorithm**. Using the segregated algorithm will solve the governing equations sequentially and individually for the solution variables, hence the name Segregated Algorithm. It is memory-efficient since the discretized equations only need to be stored one at a time. The drawback of solving the governing equations individually and sequentially however, is that the solution tends to converge quite slow. The Coupled Algorithm solves the momentum and pressure-based continuity equations as a coupled system, thus eliminating the sequential and individual calculations that were used in the Segregated Algorithm. This also means that the solution converges faster, but the use of memory increases up to two times. In Figure 4.5 a flowchart is depicted, which shows the steps involved in the iterative solution method. [30]

5 Modelling

The model, as previously stated, is based on the work by Gu, Zhong, and Yu [2] and investigates a 100 kW CFB boiler. The experimental data referenced in [2] is derived from the findings presented in [1]. This chapter provides a description of additional information and input parameters for the simulation. Firstly, some properties of the combusting particle need to be calculated and corrected accordingly. Also, the injection of particles, combustible and non-combustible solids, needs to be specified and lastly, inlet conditions of air is given and a time step is defined.

5.1 Properties of Combustibles

To ensure correct results from the combustion, some properties need to be corrected. Among these properties is the heat capacity of the volatile matter, as this should be dependent on the temperature. Additionally, the molecular weight and enthalpy of formation of the solid coal is to be specified from the ultimate and proximate analyses in Table 4.2.

5.1.1 Heat Capacity of Volatiles

FLUENT® does not account for the temperature dependence of the Cp value and the variation with temperature for the gaseous species. To take this into account a polynomial regression was made using tabulated values for the heat capacity (Cp) of methane at different temperatures. A temperature interval between 300-3000 [K] is found to be sufficient for this particular case, where the Cp value ranges from 2229 to 7079 [$J/kg \cdot K$]. [34]

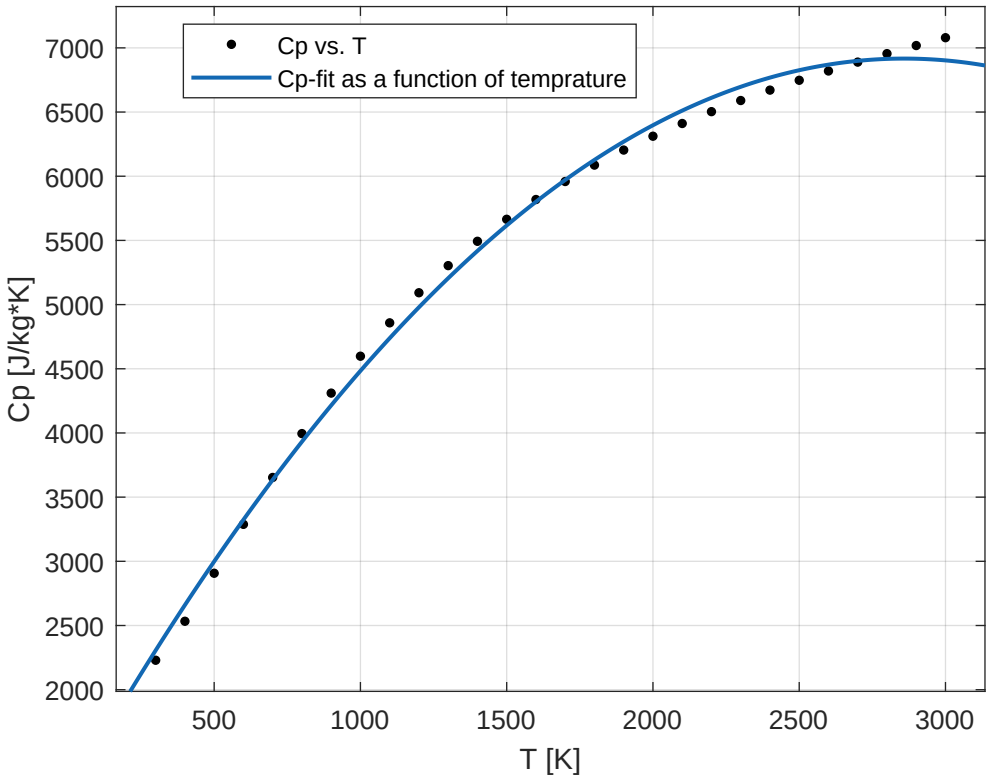

Figure 5.1: Cp value of methane as a function of temperature

A second-degree polynomial was found to be sufficient to correctly describe the relation between Cp-value and temperature. The values for the specific heat of methane were found as tabulated data in [34].

$$\mathrm{Cp}_{(T)} = -7.0418\,\mathrm{e}-04 \cdot T^2 + 4.0261 \cdot T + 1.1617\,\mathrm{e}+03 \tag{5.1}$$

It is to be noted that this polynomial should only be used in the interval of 300-3000 [K] where a R^2 value of 0.995 is guaranteed.

5.1.2 Molecular Weight of Coal

The calculation of the molecular weight is based on the proximate and ultimate analyses in Table 4.2. It is clear that the ultimate analysis does not add up to 100%, as the ultimate analysis is AR. In order to calculate the molecular weight we need to convert it from AR to *dry ash-free* (DAF). To do this the fixed carbon and volatiles from the proximate analysis are used to upscale the species in the ultimate analysis. For n species in the ultimate analysis

Equation 5.2 is used to determine the DAF composition.

$$DAF(n) = \left(\frac{n}{FC + V}\right) 100 \tag{5.2}$$

Resulting in a new ultimate analysis (DAF, *wt%*):

$$C = 80.95, \quad H = 5.20, \quad O = 11.96, \quad N = 1.9$$

To calculate the molecular weight of the volatiles, consisting of Carbon, Hydrogen, Oxygen and Nitrogen, the molecular weight of each species is used and the resulting moles is found for each species. The values are shown in Table 5.1 below. The kg/kg DAF for carbon is calculated from the carbon in the ultimate analysis (DAF) and the carbon and volatiles in the proximate analysis (AR):

$$\frac{kg}{kg} DAF_C = UA_C - \frac{PA_C}{PA_C + PA_V} 100 \tag{5.3}$$

here UA refers to the ultimate analysis and PA to the proximate analysis, while the subscript C is for carbon.

Table 5.1: Results from the ultimate analysis DAF.

Ultimate analysis (DAF, *wt%*) kmol per species.	
Carbon:	1.59
Hydrogen:	5.20
Oxygen:	7.47e−01
Nitrogen:	1.35e−01

This also results in following approximation of the volatiles stochiometry:

$$CH_xO_yN_z = CH_{3.27}O_{0.47}N_{0.09} \tag{5.4}$$

Where the stoichiometry coefficient of carbon is equal to one. The stociometry results in a molecular weight of 23.97 [kg/kmol].

5.1.3 Enthalpy of Formation of Coal

In order to calculate the enthalpy of formation, the resulting stoichiometry coefficients are used from the previous section, the following chemical reaction have to be balanced:

$$CH_xO_y + a\,O == b\,CO_2 + c\,H_2O \tag{5.5}$$

The coefficients x, y and b are known while a and c are calculated to be 1.58 and 1.63 respectively. Additionally, the lower heating value (LHV) of the volatiles have been calculated based on the proximate analysis in Table 4.2. The resulting LHV is 2.96e−01 [MJ/kg] which corresponds to 8.24 [kWh/kg]. For calculation purposes the LHV is considered in the units [kJ/kmol], since this is the unit for the enthalpy of formation in FLUENT®. The enthalpy of formation is calculated by:

$$h_{of,vol} = bh_{of,CO_2} + ch_{of,H_2O} + LHV \tag{5.6}$$

this equals an enthalpy of formation of the volatiles of −7.74e−01 [MJ/kmol].

5.2 Injections

For the injection of the combusting coal particle, the mass flow rate has to be specified to meet the thermal input of 100 kW. This is calculated based on the lower heating value, since water remains in vapor form, and the output specified. Based on the heating value calculated, the coal mass flow rate can be calculated by:

$$\dot{m}\,[kg/s] = \frac{\frac{Output}{LHV}}{3600\,[s/h]} \tag{5.7}$$

which equals a mass flow rate of coal of 3.5e−03 [kg/s]. Information on the defined variables in the coal injection can be seen in Table 5.2.

Table 5.2: Properties of coal as used in this project.

Coal injection			
Diameter range [m]	Mass flow rate [kg/s]	Density [kg/m^3]	Injection temperature [K]
3.55e−04 : 4e−3	3.5e−03	1300	300

The injection of particles are created as file injections, the method of file injection is described in Section 3.4.1. The injection of particles are divided into four injections volumes, where one injection is for the riser and the other three are for the loop seal, in total 350000 particle parcels are injected into the domain. The material selected in the FLUENT® software is *ash-solid*, and the material properties are changed to fit the particles in [2], the particle properties and important parameters for injection can be read in Table 5.5.
To determine the correct injection mass of the particles it is calculated based on the necessary volume fraction, the volume fraction of the discrete phase is read from Figure 7.a in [2]. In the riser the volume fraction of the discrete phase is seen to be $\alpha \approx 0.3$ while in the loop seal it is $\alpha \approx 0.55$. The mass of particles to be injected is calculated by:

$$m = \rho V \alpha \tag{5.8}$$

The volumes for the injections are stated in Table 5.3 below. Here the riser injection volume is based on the diameter stated in Table 3.1.

Table 5.3: The calculated volume for each injection.

Injection volumes [m^3]	
Riser injection	5.77e−03
Loop seal injection one	19.3e−04
Loop seal injection two	7.84e−04
Loop seal injection three	7.73e−04

The injection volumes are calculated from the bounding geometries given in Table 5.4.

Table 5.4: The bounding geometry for each injection. Where the riser is bounded by a cylinder and the loop seal injections are bounded by squares.

Riser injection, cylinder [m]	
r=3.5e−02	h=1.5 ($y = 0 : 1.5$)
Loop seal injections, square [m]	
Loop seal injection one:	$x = 6.15\text{e}{-01} : 8.69\text{e}{-01}$
	$y = 1.01 : 1.11$
	$z = -4.0\text{e}{-02} : 4.0\text{e}{-02}$
Loop seal injection two	$x = 6.15\text{e}{-01} : 6.85\text{e}{-1}$
	$y = 1.11 : 1.25$
	$z = -4.0\text{e}{-02} : 4.0\text{e}{-02}$
Loop seal injection three	$x = 8.01\text{e}{-01} : 8.70\text{e}{-01}$
	$y = 1.11 : 1.25$
	$z = -4.0\text{e}{-02} : 4.0\text{e}{-02}$

In the injection script the total mass is then defined as in Equation 5.8, while the mass flow in the injection file is calculated by:

$$\dot{m} = \frac{\frac{m}{t_{stop}}}{N_{parcels}} \tag{5.9}$$

where t_{stop} is the defined stop time for the injection in the injection window in FLUENT®, set to 1e−08 [s]. Additional information on the bed material injections is given in Table 5.5. The file injections of the bed material are on the form given in Equation 3.1, where the position (x,y,z) is randomly chosen within the given bounded geometry of each injection, as shown in Table 5.4, and the velocity components are set to zero.

Table 5.5: Important information on the injections of the bed material.

Riser injection			
Diameter:	Mass flow rate:	Density:	Injection temperature:
2e−03 [m]	3e+03 [kg/s]	2600 [kg/m^3]	1123 [K]
Loop seal injection one			
Diameter:	Mass flow rate:	Density:	Injection temperature:
2e−03 [m]	2.76e+03 [kg/s]	2600 [kg/m^3]	300 [K]
Loop seal injection two			
Diameter:	Mass flow rate:	Density:	Injection temperature:
2e−03 [m]	2.24e+03 [kg/s]	2600 [kg/m^3]	300 [K]
Loop seal injection three			
Diameter:	Mass flow rate:	Density:	Injection temperature:
2e−03 [m]	2.21e+03 [kg/s]	2600 [kg/m^3]	300 [K]

5.2.1 Injection Summary

Important injection information are summarized in Table 5.6.

Table 5.6: Summarized injection information, where the type of injection, location of injection, injection material, injection diameter and mass flow rate calculations are provided.

Injection	Type	Location	Material	Size [m]	Mass flow rate
Riser	File	Bottom of riser	Inert particle	Uniform D=2e−03	Calculated by Equation 5.9
Loop seal 1	File	Bottom of loop seal	Inert particle	Uniform D=2e−03	Calculated by Equation 5.9
Loop seal 2	File	Top left of loop seal	Inert particle	Uniform D=2e−03	Calculated by Equation 5.9
Loop seal 3	File	Top right of loop seal	Inert particle	Uniform D=2e−03	Calculated by Equation 5.9
Coal	Surface	Coal inlet (See Figure 3.1)	Coal_lv, combusting particle	Varying D=3.55e−04: 4e−03	Calculated by Equation 5.7

The locations defined in Table 5.6 is visualized in Figure 5.2.

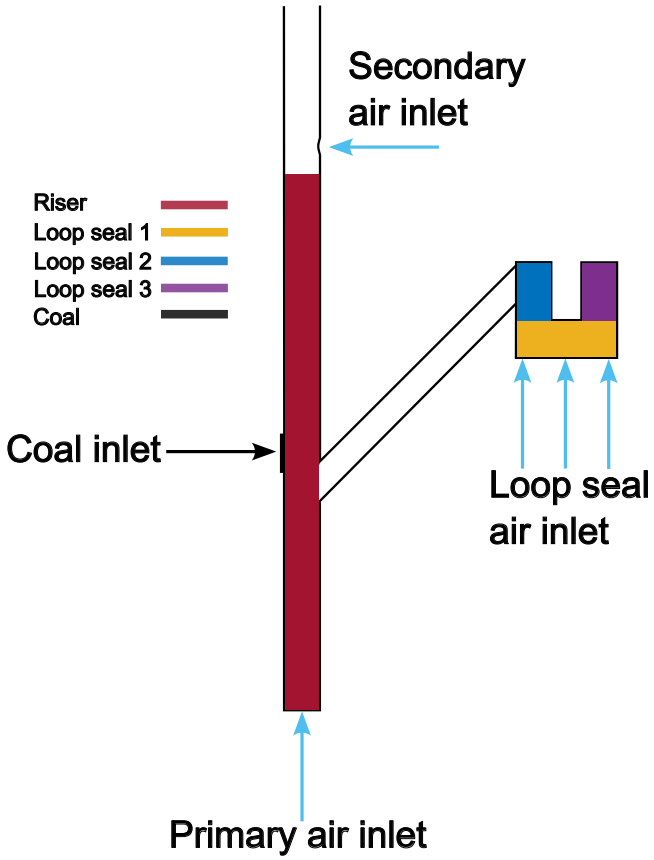

Figure 5.2: Visualisation of the injection locations as described in Table 5.6.

5.3 Inlet Conditions of Air

In Table 5.7 below the air inlet conditions can be read. The species defined in the inlet air is 35% oxygen and 65% carbon dioxide, similar to Gu, Zhong, and Yu [2]. The absence of inlet conditions of air at the coal inlet is due to the assumption that it is mechanically fed into the boiler.

Table 5.7: Flow rate and temperature of air inlets.

Primary air inlet	
Volumetric flow rate [m^3/h]:	47.8
Temperature [K]:	473.15
Secondary air inlet	
Volumetric flow rate [m^3/h]:	20.01
Temperature [K]:	473.15
Loop seal air inlet	
Volumetric flow rate [m^3/h]:	2.4
Temperature [K]:	300

5.4 Convergence Criteria

When determining convergence, a common practice is to monitor the residuals. Additionally, an important parameter to consider, in regards to convergence, in CFD simulations is the Courant number.

Courant Number

The Courant-Friedrichs-Lewy (CFL) condition in a 3D grid is defined as([35])

$$C = \Delta t \sum_{i=1}^{3} \frac{u_{x_i}}{\Delta x_i} \leq C_{max} \tag{5.10}$$

where C is the Courant number. The Courant number is defined as the number of cells travelled by the flow in one time step, illustrated in Figure 5.3. It is important to note that it is generally of interest to keep the Courant number at or below unity, but explicit simulations are typically more sensitive to this condition than implicit solvers.

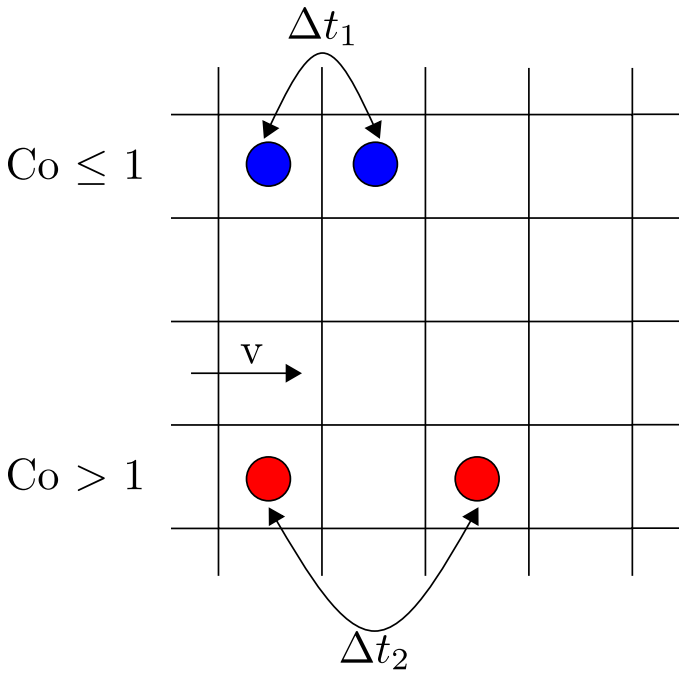

Figure 5.3: Visualisation of the CFL condition, where the Δt_1 indicates a Courant number below or equal unity and therefore the CFL condition is met. While for Δt_2 the condition is not met.

6 Results

The results will be presented in the following order:

- **GCI:** Cold air flow
- **Case 1:** Particle distribution
- **Case 2:** Combustion

The conditions which the simulations are run under is presented in Table 6.1 below.

Table 6.1: Models activated for the cases described.

Case	Multiphase	Turbulence	Energy	Combustion
GCI	Off	On	Off	Off
Case 1	On	On & Off	Off	Off
Case 2	On	On	On	On

Besides the cases, the phases are important to differentiate between since these will be referred to as phase one, phase two and phase three. The phases are defined as presented in Table 6.2

Table 6.2: Description of the phases.

Phase one	Phase two	Phase three
Primary phase (air)	Discrete phase (inert)	Discrete phase (combusting)
	Sand	Coal

In the upcoming sections the results from the cases will be presented, but before the results from cases are presented a Grid Convergence Index (GCI) study is performed to evaluate the accuracy of the computational mesh generated. At the end of the GCI study a timestep is chosen, based on the CFL condition and considering a C_{max} value of unity.
In the results from **case 1** the impact of turbulence on the particulate phase distribution will be investigated. Also, the DPM model with and without DEM is to be compared since

the DEM model is suggested by Ansys Fluent for simulation of CFB boilers with a high particle loading, but due to increased computational time it is not preferred.
Additionally, the results from **case 2** will be presented in a chronological order, where small changes are made to the computational settings, which will be clearly stated, in an attempt to obtain results matching the experimental data from Li et al. [1]. The experimental results from Li et al. [1] will be presented before the results from simulations in **Case 2**.
Lastly, the chapter will be ended with a summary of the results, which is compared to the experimental data.

6.1 Grid Convergence Index

To perform the grid refinement study in this project, the grid convergence index (GCI) method proposed by Roache [36] is used. This method is based upon a generalized Richardson Extrapolation, with n^{th}-order methods and e-value of grid ratios, where the exact solution is approximated by:

$$f_{\text{exact}} \cong f_1 + \frac{f_1 - f_2}{e^n - 1} \tag{6.1}$$

In Equation 6.1 e is the grid refinement ratio, which in [36] is recommended to be ≥ 1.1, in this project it is approximately 1.2 in order to ensure convergence. The grid refinement is calculated using the grid spacing, h, which is calculated using Equation 6.2.

$$h_i = \left(\frac{1}{N_i} \sum_{j=1}^{N_i} \Delta V_j \right)^{1/3} \tag{6.2}$$

Where V_j is the volume of each cell. The difference between the computed and continuum value for the fine grid is used to calculate the GCI in Equation 6.3. Where F_s is a safety factor, which has a value of 1.25 for comparisons of three or more grids.

$$GCI_{\text{fine}} = \frac{F_s \cdot \left| \frac{f_1 - f_2}{f_1} \right|}{(e^n - 1)} \tag{6.3}$$

The order of accuracy, n, in Equation 6.1 is defined in Equation 6.4, which is solved iterative.

$$n = \frac{ln\left|\frac{f_3 - f_2}{f_2 - f_1}\right| + ln\left(\frac{e_{21}^n - s}{e_{32}^n - s}\right)}{ln(e_{21})} \tag{6.4}$$

Where s is defined using a sign function:

$$s = sign\left(\frac{f_3 - f_2}{f_2 - f_1}\right) \tag{6.5}$$

The result from the GCI can be seen in Table 6.3 below, here the deviation is based on the extrapolated value. The GCI value from Equation 6.3 for the fine mesh results in a calculated deviation of $\approx 4.3\%$, which is a bit higher than the value in the table due to the safety factor.

Table 6.3: Results from the GCI study.

Coarse grid	
Number of cells:	284551
Differential pressure (Pa):	376.97
e:	-
Deviation [%]:	7.35
Medium grid	
Number of cells:	481762
Differential pressure [Pa]:	371.54
e:	1.19
Deviation [%]:	5.89
Fine grid	
Number of cells:	799265
Differential pressure [Pa]:	362.69
e:	1.18
Deviation [%]:	3.49

Additionally, the results are plotted in Figure 6.1.

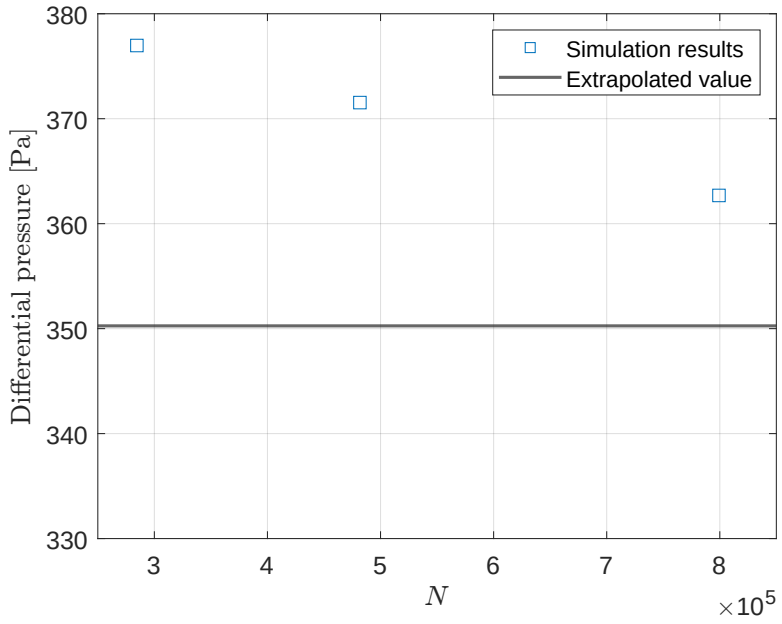

Figure 6.1: GCI results for the three grids examined with differential pressure between inlet and outlet on the y-axis and number of cells, N, on the x-axis.

Due to the scope of this project, and the limited time for completion, the coarse mesh is used for simulations. Therefore, the results from the simulations are expected to deviate from the exact solution.

The time step is determined from the velocity stated in Table 5.7 and based on the coarse mesh with $\approx$ 285e+03 cells. The time for the flow to traverse a single cell, based on an average cell side length, is calculated by:

$$\Delta t = \frac{\sqrt[3]{\frac{V_{total}}{n_{cells}}}}{v} \tag{6.6}$$

With the highest injection velocity being the secondary air of $v \approx 4.4$ [m/s] the equivalent Δt becomes 1.85e$-$03 [s]. In order to ensure convergence, and the fullfillment of the CFL condition, the time step is chosen to be $\Delta t = 1.0\text{e}{-}03$. All simulations are run in transient with a number of time steps equal to 10e+03, resulting in a simulated flow time of 10 seconds, which resulted in a computational time of $\approx$ 100 hours.

6.2 Case 1

For case one concerning the particle distribution the post processing option in FLUENT® is chosen to be the particle tracking, since this provides the best visualization of the particulate phase distribution. Though, to illustrate the volume fraction, which the simulation is initialized with, the standard contour plot is chosen.
The first time step of the simulation is executed to inject the particles, and the initial volume fraction is illustrated in Figure 6.2. Here the volume fraction is approximately $\alpha \approx 0.3$ and $\alpha \approx 0.55$ for the riser and loop seal respectively, as calculated in Section 5.2.

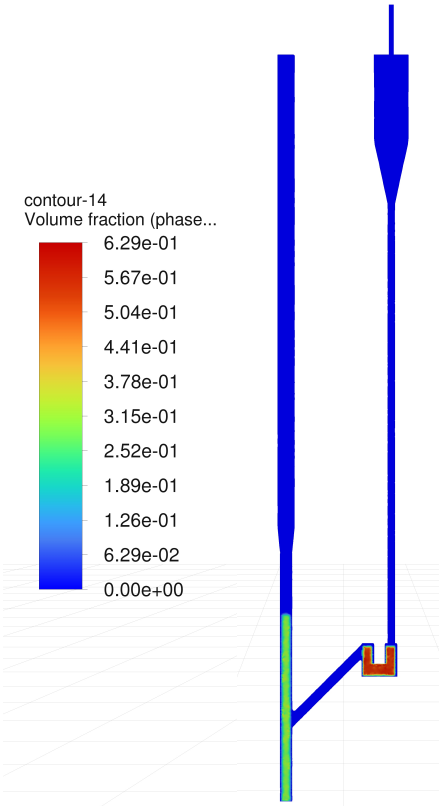

Figure 6.2: Contour plot colored by volume fraction in a plane cut of the geometry. (t=1e−3s)

Additionally, the initial volume fraction can be seen using particle tracking coloured by the volume fraction in Figure B.7 in Appendix B.1.
In Figure 6.3 it is clear that the particles are packed together in the bottom of the riser resulting in a high volume fraction in this area. While there is a relatively low volume fraction in the downcomer and barely any particle distribution along the riser height.

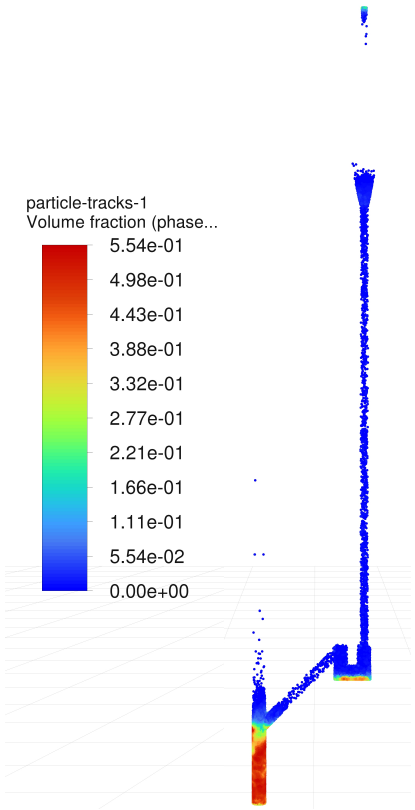

Figure 6.3: Particle tracking colored by volume fraction in simulation without turbulence. (t=10s)

The simulations were then run with turbulence included and the resulting particle tracking colored by volume fraction can be seen in Figure 6.4a, and compared to Figure 6.3 a larger distribution of particles throughout the riser height is observed. This distribution is observed to become significantly larger when the DEM is enabled in Figure 6.4b. The DEM should more precisely track the particles when the particle loading is high, but it seems to overestimate the distributions which might be due to the spring-dashpot term. In the simulation with DEM activated in Figure 6.4b the default settings for the spring-dashpot terms are retained, which results in a relatively high spring constant of 1000 [N/m].

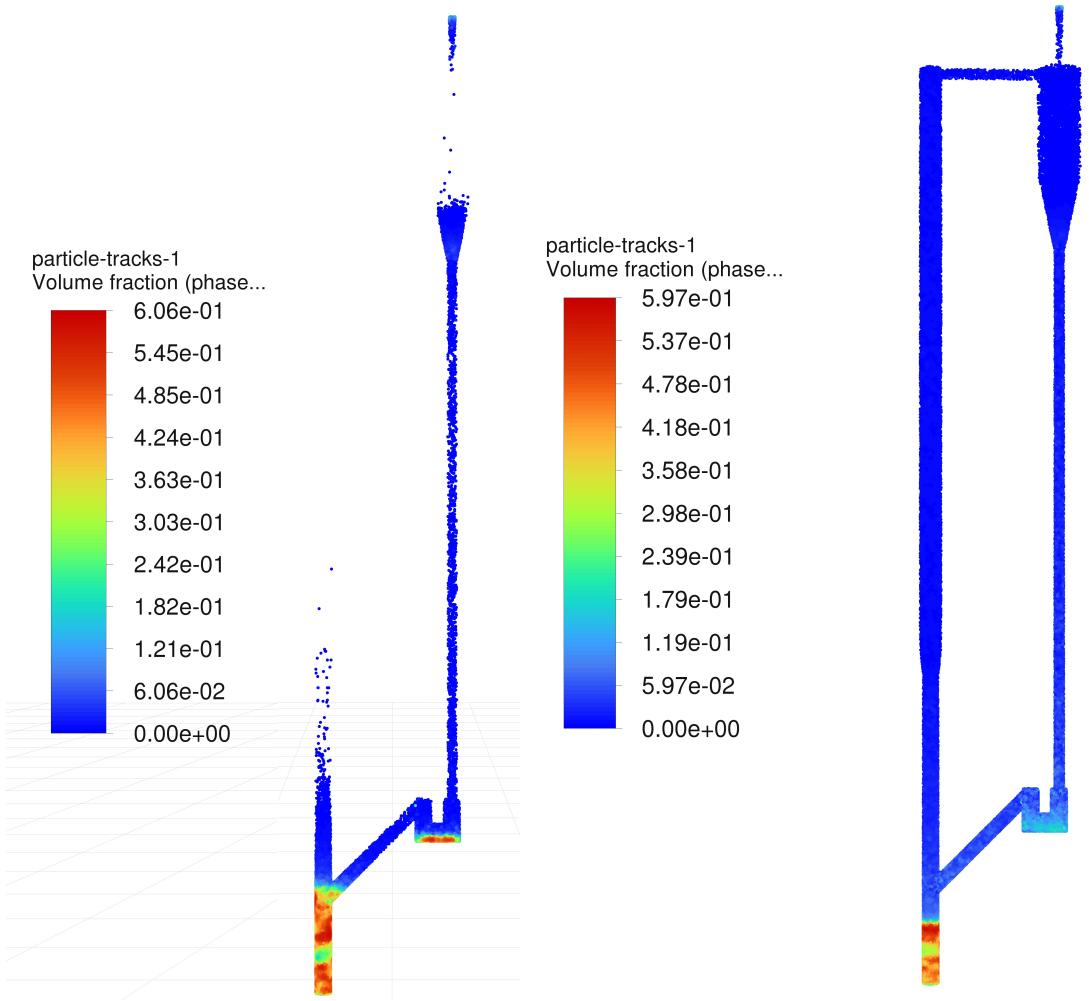

(a) Without DEM. (t=10s) **(b)** With DEM. (t=10s)

Figure 6.4: Particle tracking colored by volume fraction with turbulence activated. Without DEM (a) and with DEM (b).

Additionally, the spring constant was reduced with a factor of 10 and the results from this simulation can be seen in Figure 6.5. It is obvious from the particle tracking, that an increased spring constant results in increased particle distribution. This indicates that the distribution is highly dependent on particle-particle and particle-wall collisions and the resulting force from these.

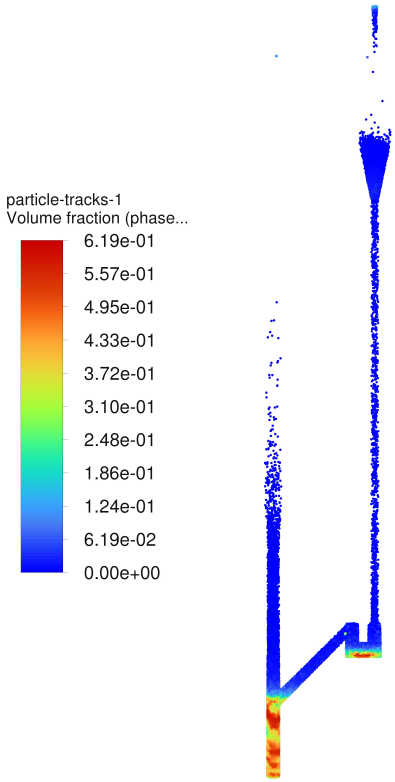

Figure 6.5: Particle tracking coloured by volume fraction with DEM and turbulence activated. The spring constant and dashpot efficiency is reduced. (t=10s)

The increased computational precision comes at a cost of increased computational time. For the simulation with DEM activated the resulting computational time increase was approximately 20%, which corresponds to an added time of ≈6 hours. Due to the increased computational time and the uncertainties on the spring-dashpot values, the DEM is not preferred in further simulations.

6.3 Case 2

The goal of the simulations in case two is to obtain results similar to the experimental results of Li et al. [1]. The temperature measured along the riser in the experiment are presented in Figure 6.6.

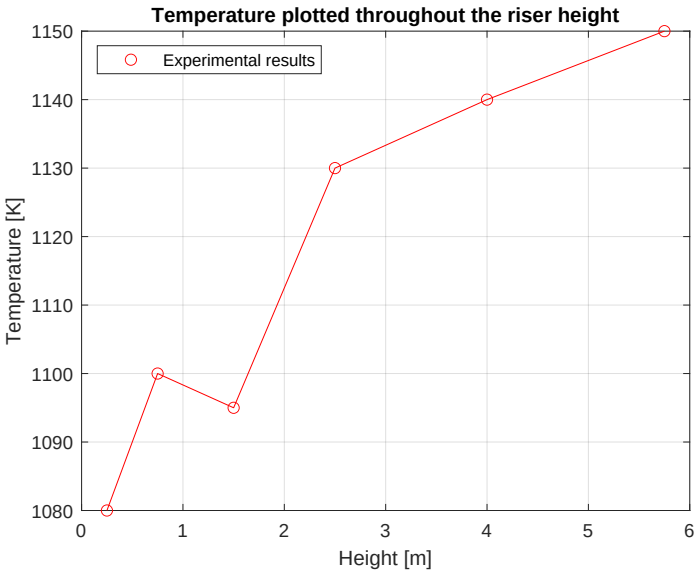

Figure 6.6: Results of temperature throughout the riser height from Li et al. [1].

The simulations including combustion are run using the settings as described in Chapter 3. Additionally, the post processing in FLUENT® for case two is chosen to be the pathlines option, since this better depicts the entire 3D domain as compared to the standard contour plot.

6.3.1 Simulation 1

In Figure 6.7 the pathlines of phase one and two are plotted and colored by temperature. The temperature is seen to have a similar distribution in both phase one and two, though it is also observed to be low considering combustion is ongoing. The maximum temperature can be observed to be 745 K, but in the experimental results from [1] a maximum temperature of ≈1200 K is reached. The temperature of the particle parcels was set to 1123 K while the region of the injection ($y = 0 \rightarrow y = 1.5$) was patched to the same temperature of 1123 K. As the simulation proceeded, it was observed that the temperature decreased from the start to the end of the simulation, which indicates that it might continue to decrease if the simulation was run for a longer duration.

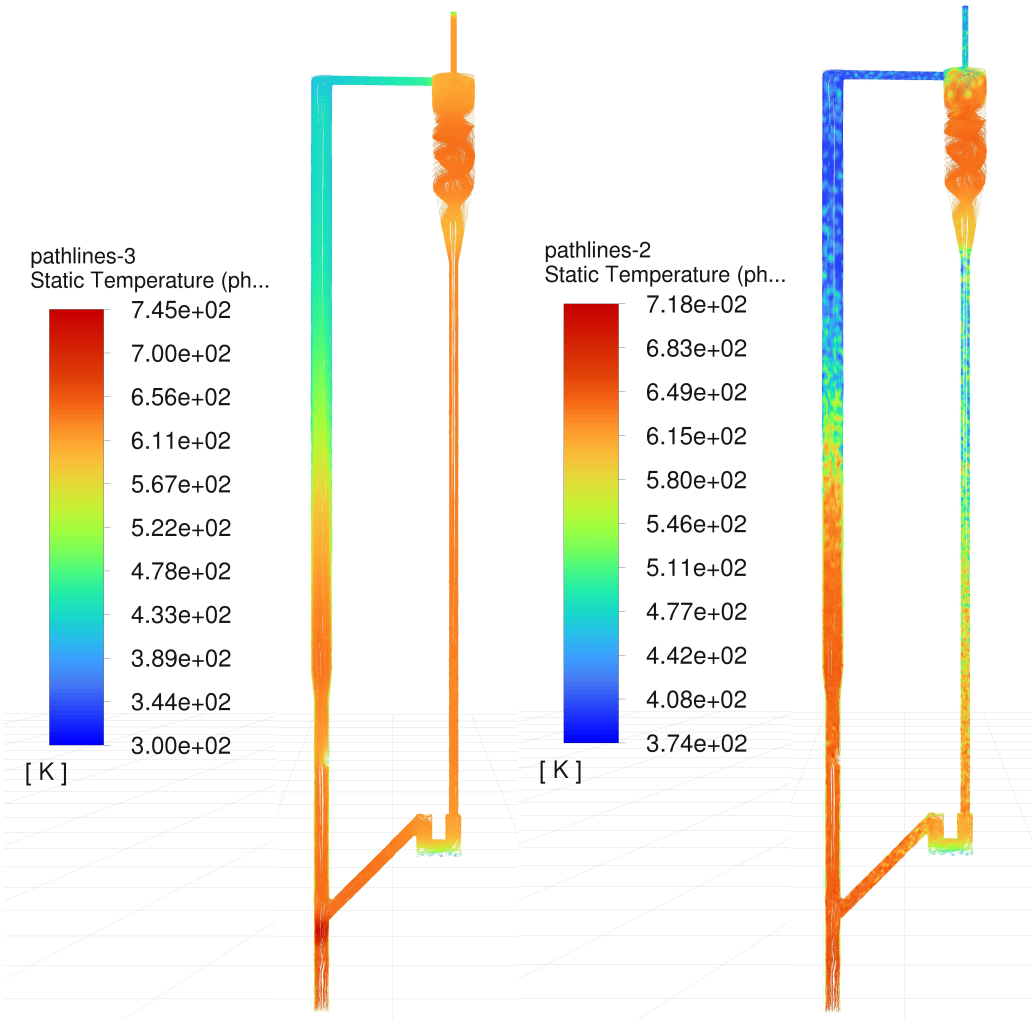

(a) Phase one temperature. (t=10s)

(b) Phase two temperature. (t=10s)

Figure 6.7: Pathlines colored by temperature from simulation with combustion enabled showing phase one (a) and phase two (b).

A similar tendency in the temperature is observed for the combusting phase in Figure 6.8a and the volume fraction in Figure 6.8b indicates a small distribution of the combusting particle. The small distribution should not pose problems, since the bottom region of the riser experiences the highest temperature.

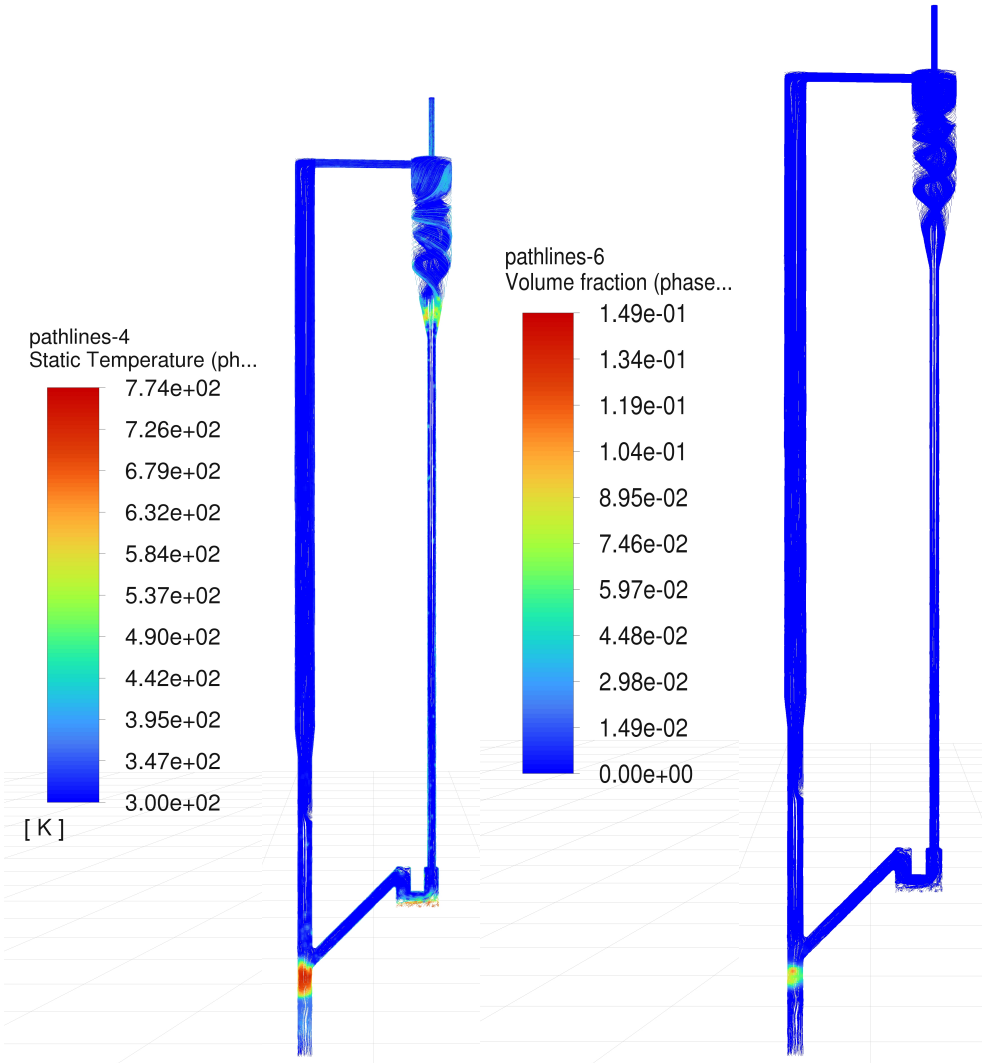

(a) Phase three temperature. (t=10s) **(b)** Phase three volume fraction. (t=10s)

Figure 6.8: Pathlines of phase three colored by temperature (a) and volume fraction (b) from simulation with combustion enabled.

The low temperature could be problem induced by the volatiles which might not be combusting. In Figure 6.9 pathlines of the volatiles colored by mass fraction is seen, where the mass fraction at the outlet was expected to be zero. This was expected as it should be combusting, and the existence of volatiles at the outlet could indicate that the volatiles is not combusting.

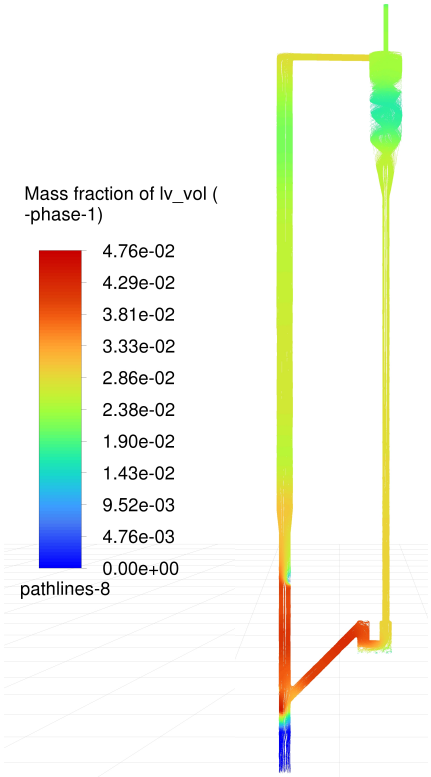

Figure 6.9: Pathlines of volatiles colored by mass fraction. (t=10s)

Since the temperature is decreasing so is the kinetics as these are calculated using the Arhenius equation (Eq. 4.41), and it is dependent on the temperature. When using the finite rate model in combination with the eddy/dissipation model, the reaction rate is chosen as the slowest of the two models.

6.3.2 Simulation 2

In order to investigate if the temperature is the variable causing the slow rate of reaction, a simulation is run using only the eddy/dissipation model. The results from the simulation using the eddy-dissipation approach can be seen in Figure 6.10. It can be observed from the pathlines in Figure 6.10b that the volatiles are combusting, since there are no volatiles present at the outlet as it was observed in Figure 6.9. Additionally, the temperature is seen to be higher and more uniform throughout the domain as compared to Figure 6.7a. The highest temperature is observed at the primary air inlet, where the volatiles are still present and combusting.

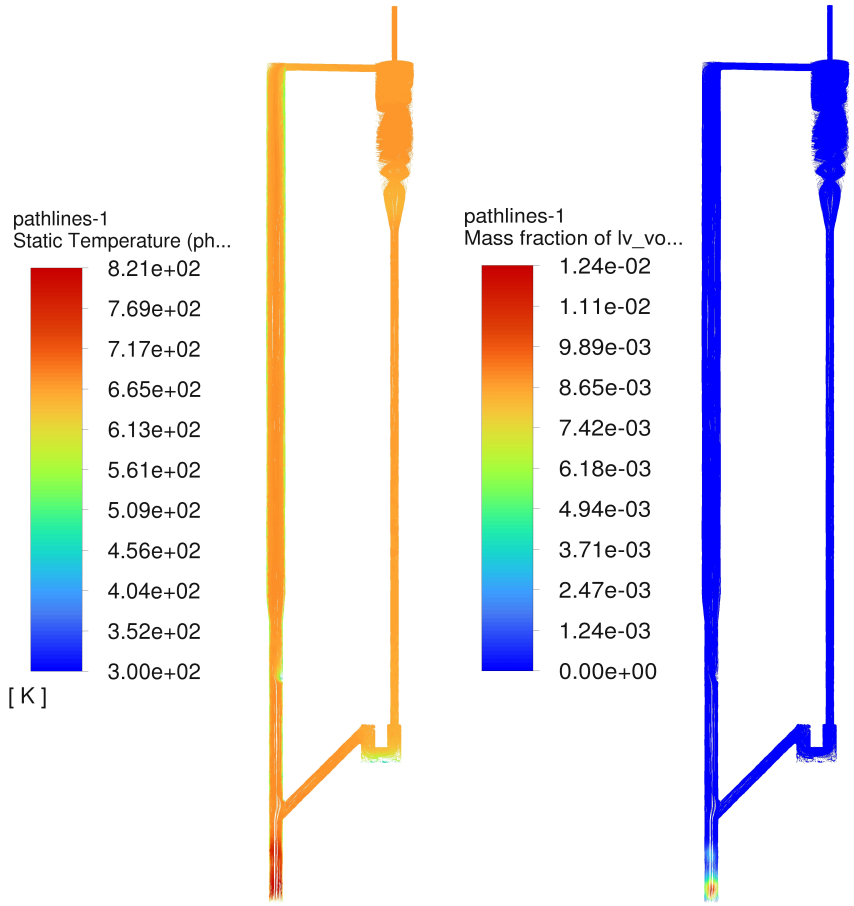

(a) Primary phase temperature (t=10s) **(b)** Mass fraction of volatiles (t=10s)

Figure 6.10: Pathlines of primary phase colored by temperature (a) and pathlines of volatiles colored by mass fraction (b) from simulation with the Eddy-Dissipation approach.

As the temperature is still observed to be rather low in Figure 6.10a, compared to the wanted temperature of ≈1200 [K], the coal temperature is increased in an attempt to accelerate the devolatilization.

6.3.3 Simulation 3

Keeping the eddy dissipation model, since the temperature was observed to be higher and the volatiles combusting, the inlet temperature of coal is increased to 600 [K]. From the result presented in Figure 6.11a it can be observed that a higher temperature is obtained in the domain, but it does not seem to have increased significantly as wanted throughout the riser. Additionally, Figure 6.11b shows the volatile mass fraction to be non existing at the

outlet, confirming, as in Figure 6.10b, that the volatiles are combusting.

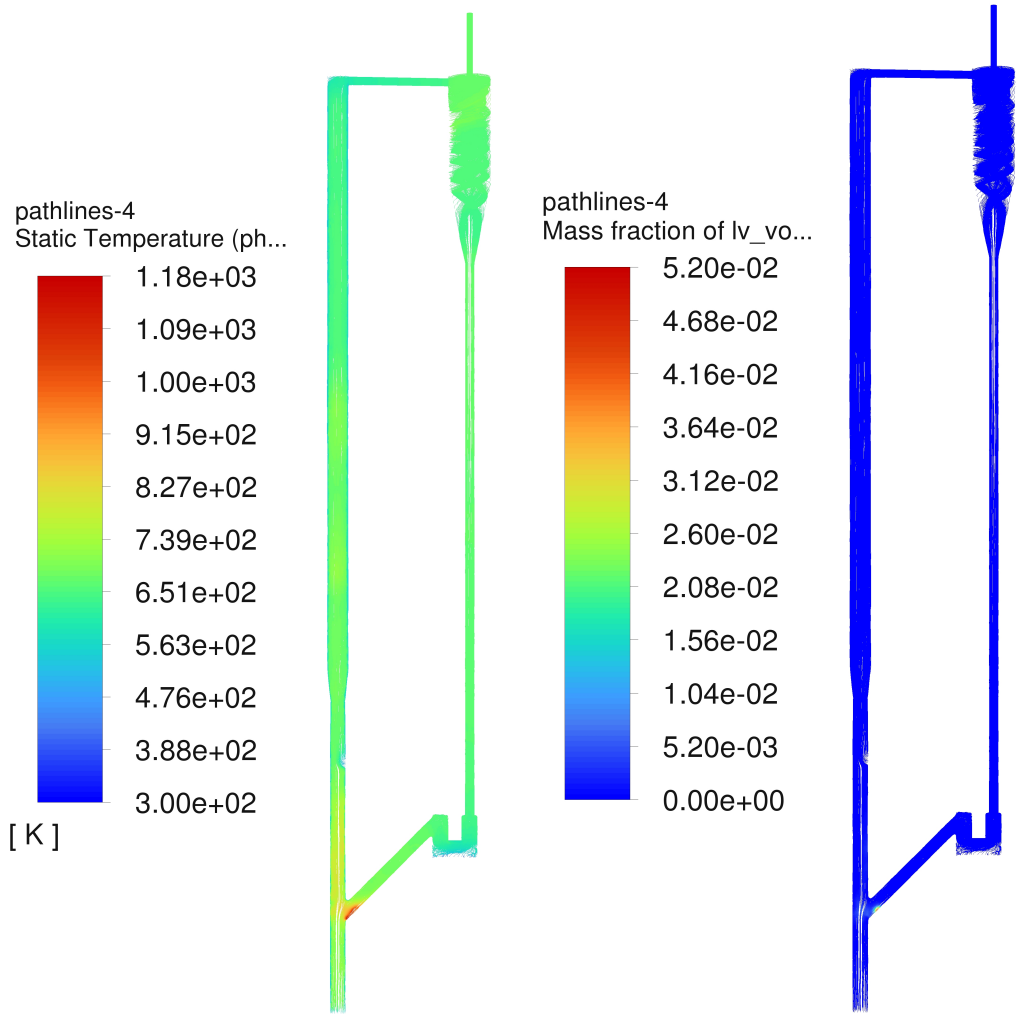

(a) Primary phase temperature (t=10s)

(b) Mass fraction of volatiles (t=10s)

Figure 6.11: Pathlines of primary phase colored by temperature (a) and pathlines of volatiles colored by mass fraction (b) from simulation with the Eddy-Dissipation approach.

Since the temperature is not near the temperatures measured in the experimental data from Li et al. [1], and the volatiles are seen to be combusting, the cause of the temperature difference should not be related to the combustion processes. One factor which could be the root of the temperature difference is the simulated flow time, it was chosen to be 10 seconds in this project due to the relative small time frame.

6.3.4 Simulation 4

In order to investigate if the simulation time could be the root of the problem, an even coarser mesh is created for the sole purpose of investigating this. The created contains no boundary layers and consists of just over 80e+03 cells, this mesh is not tested in regards to accuracy like the previously generated mesh in the GCI study, the results are therefore expected to be prone to relative large errors. The computational time on the new mesh was about 36 hours to simulate a flow time of 30 seconds. Results are presented in Figure 6.12, where the highest temperature is observed to have increased by $\approx$ 200 [K] in Figure 6.12a while the same observations, as for previous results, are done in regards to the mass fraction of the volatiles in Figure 6.12b.

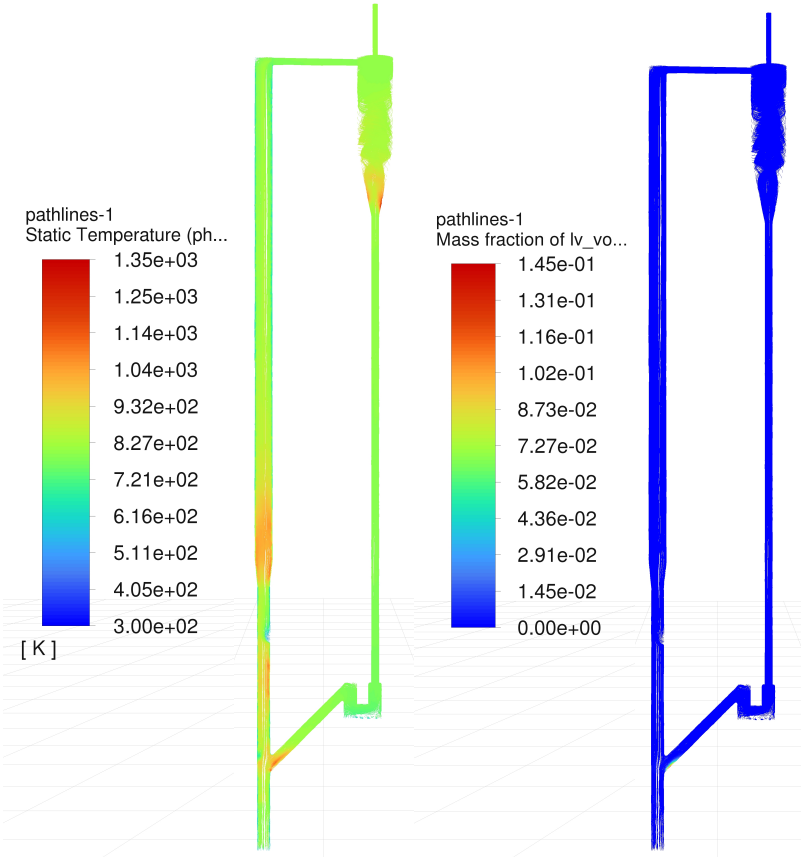

(a) Primary phase temperature (t=30s) **(b)** Mass fraction of volatiles (t=30s)

Figure 6.12: Pathlines of primary phase colored by temperature (a) and pathlines of volatiles colored by mass fraction (b) from simulation with the Eddy-Dissipation approach.

6.4 Summary of Results

At the start of Section 6.3 the results from the obtained experimental data of Li et al. [1] was presented. To summarize the results obtained in the simulations from case two, the temperature along the riser height is plotted for each simulation alongside the experimental results in Figure 6.13.

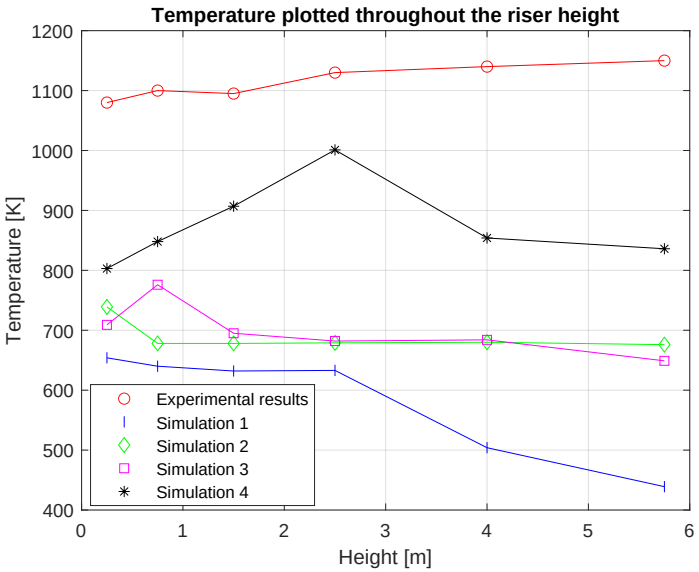

Figure 6.13: Temperature from experiments and simulations measured throughout the riser.

The values from the experimental result and from the simulations and the corresponding mean deviation from the experimental results are presented in Table 6.4 below.

Table 6.4: Temperature values from experimental results and simulations along the riser height presented along with the mean deviation of the different simulations.

Measurement height [m]	Experimental results [K]	Simulation one [K]	Simulation two [K]	Simulation three [K]	Simulation four [K]
0.25	1080	654	739	709	803
0.75	1100	640	478	776	848
1.5	1095	632	678	695	907
2.5	1130	633	679	682	1001
4.0	1140	504	680	684	854
5.75	1150	439	676	649	836
Deviation [%]:	-	47.7	38.3	37.3	21.6

Based on the results plotted in Figure 6.13 and presented in Table 6.4 it is clear that the deviation for simulation two and three, where the combustion of the volatiles was observed to be undergoing, is almost equal even though it was attempted to accelerate the combustion by increasing the temperature of the injected coal. Whereas, simulation four provided the smallest deviation, which indicated that the issue could be posed by the shorter simulation time in the prior simulations.

7 Discussion

7.1 Meshing

A very common error that occurred continuously was the '**floating point exception'-error**'. This generally means that somewhere in the iterative solution method, a number is divided by zero, and can often be related to meshing quality. Another error that occurred quite frequently is the '**temperature is limited to xxx in xxx cells**', the cause of this error is unknown, but most likely it is related to the models and settings in some way. For some meshes, the addition of boundary layers proved to be problematic, since the boundary layer cells were very skewed and had a very high aspect ratio near some edges. It was especially problematic in edges and corners where the angle is ≥ 90 °. To solve this problem, several edges were rounded. A depiction of one of the edges which was deemed problematic and the resulting rounded edge can be seen in Figure 7.1.

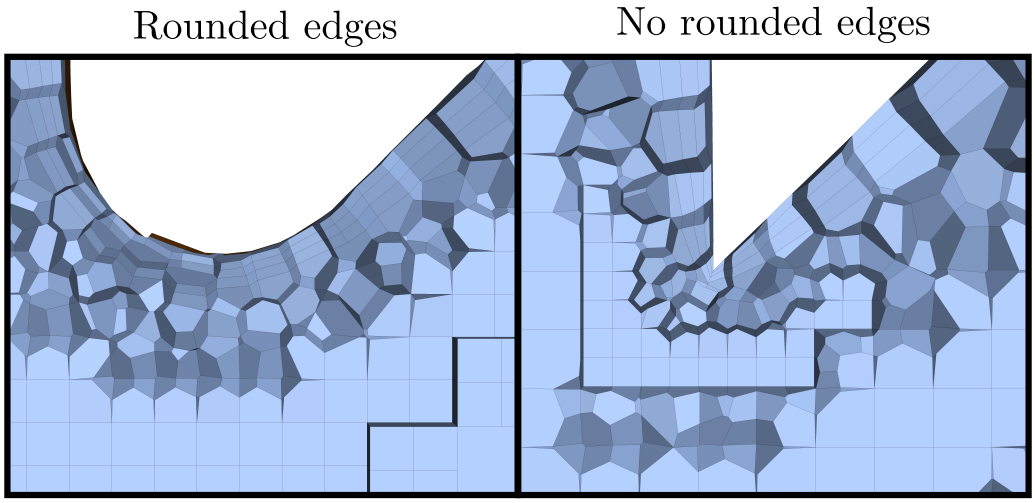

Figure 7.1: A figure depicting the mesh with and without rounded corners.

7.2 Turbulence

When multiphase flow is run with turbulence enabled, there is an option for the treatment of the turbulence to be either mixture or dispersed. If there is a clear continuous phase, as

in the case of this project, the dispersed option should be used. The use of the dispersed option resulted in diverging simulations, even though all other settings was kept the same. It was attempted to reduce the time step, but this caused the simulation to diverge after fewer iterations. The cause is unknown, but is likely related to the discrete phase, where the volume fraction might be too high. The divergence was caused by a "spike" in the epsilon residual from the turbulence model as seen in Figure 7.2, where Figure 7.2a is simulated using a time step of 1e−3 s and Figure 7.2b is with a time step of 5e−4 s.

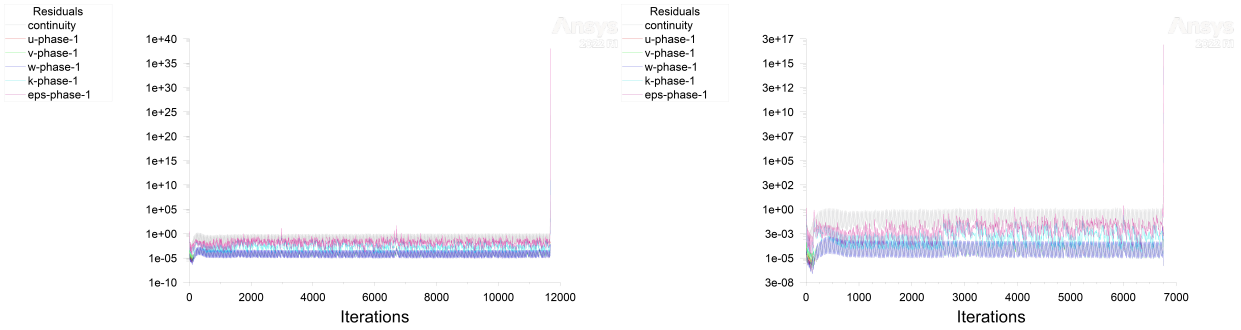

(a) **(b)**

Figure 7.2: Residuals for simulations of multiphase flow with a time step of (a) 1e−03 s and (b) 5e−04.

7.3 Discrete Phase Model

The injection of the particles posed a lot of problems throughout the project period. The initial approach was to use the volume injection, since this injection type let the user define a volume fraction within a bounding geometry. Firstly, this injection type proved to be incompatible with the DEM physical model, and it also proved to be difficult to control the number of particles. The resulting injection, when defining a volume fraction, was injecting tens of millions of particles which required more memory than the available 256 Gb, ultimately causing the simulation to crash. For this reason the file injection was utilized instead.

7.3.1 Discrete Element Model

According to [30] the DEM provides more accurate results from particle collisions and is proposed for flow with a high particle loading, like in a CFB boiler. In the model window

of collision pairs when activating the DEM a number of constants is to be specified such as the spring constant. The spring constant is estimated by Equation 4.14, where the relative velocity and allowable deformation is used. As the flow is primarily one dimensional in the riser, the relative velocity between particles should not become too large resulting in a low spring constant. Assuming a value for the relative velocity of 10 m/s and an allowable overlap of 0.1D the resulting spring constant is ≈21. This assumed value of the relative velocity is rather high, since the inlet velocity of the primary phase at the primary inlet is about 2 m/s. This indicates that the result from the DEM model overpredicts the particulate phase distribution, since the lowest spring constant used is $k = 100$.

7.4 Compatibility

It is important to acknowledge the compatibility between models, schemes and settings. In general, the models in FLUENT® offers great compatibility. The discrete phase model is compatible with all turbulence models, except from LES. The Eulerian model is only compatible with the following TCI models: Finite Rate/Eddy dissipation, Eddy Dissipation and the Finite Rate model. Even though FLUENT® offers great compatibility, there are combinations using turbulence-, combustion- and multiphase-models that offers less resilience. The computational time also varies depending on the combination of models used, and it can be very time consuming to determine which combinations offer the least computational time along with the most realistic results. It has not been possible to use the 'coal calculator'-setting in species transport with the Eulerian multiphase-model active. The 'Coal-calculator' option, makes it possible to adjust the stoichiometry and include components like SO_2 of the chemical reactions.

7.5 Transient and steady state

Simulations with similar settings as the one simulated in Figure 6.3 were also attempted in steady simulations, but it proved difficult to control the injection of particles and the time step of the particulate phase. Since it is only possible to perform unsteady tracking in order to account for particle-particle collisions, the steady simulation could converge before the particle tracking had reached the wanted simulation time. Results from the

steady simulation is shown in Figure B.2 and Figure B.3 in Appendix B. Where the results in Figure B.2 is after 6000 iterations and particles are seen to mainly occupy the bottom half of the domain. After more iterations the concentration of particles are seen to shift to the top half in Figure B.3, which is quite the opposite of what is observed in the transient simulations, where a dense bed is formed at the bottom of the riser. Furthermore, the particles was seen to pack in the cyclone in the steady simulation after more iterations, which is not expected and does not fit into the tendency observed in literature (as in [2]).

7.6 Simulation Time

A flow time of 10 seconds might not be proficient, and longer simulations could provide valuable insight into the transient behaviour of the CFB boiler performance. The simulation time of 10 seconds was chosen due to the time frame of the project. During the simulations it was discovered to not be sufficient simulation time to capture the final/steady temperature within the domain, due to the kinetics of the combustion processes and the relatively large geometry.

7.7 Computational Time

Simulating complex multiphase flows and combustion is computationally intensive, especially when high accuracy is desired. The most computationally demanding simulations required 4-5 days to simulate 10 seconds of flow time. The computational resources available consisted of an AMD EPYC 7543P and 256 GB of memory. When using the server computer, it was advised to run the simulation using 16 cores, which is proficient enough for most tasks. In most CFD software it is important to consider how many cells are computed per core, some claim that 10e+03 cells per core is preferred in FLUENT®, while others claim that 10e+04 cells per core is the optimum. This, however, depends on how many equations are solved. For a simulation were multiphase, combustion and turbulence is active, less cells per core could prove to be the better option.

8 Conclusion

Based on the GCI the deviation of the coarse mesh consisting of $\approx$ 285e+03 is estimated to be 7.35%. Due to the time frame of the project, the coarse mesh is used, despite having approximately twice the deviation of the fine mesh.
Furthermore, the particulate phase distribution was investigated using the approach based on both DEM and KTGF. An increase in computational time from the KTGF to the DEM approach was observed to be 20%, while the DEM also proved to be more challenging to implement due to multiple constants which had to be defined.
The combustion simulation indicate that the finite rate/Eddy dissipation TCI is causing slow kinetics, resulting in volatiles not being combusted. Since the finite rate/eddy dissipation approach determines the rate constant by both the Arrhenius equation and the turbulence and proceeds with the slowest of the two, the finite rate approach was deselected as this is temperature dependent. From the simulations using just the eddy dissipation approach it is clear that the volatiles are combusting, since the mass fraction is observed to be zero at the outlet, in contrast to simulation one. However, this accelerated combustion did not lead to a higher overall temperature across the domain as anticipated. Instead, it resulted in higher temperatures being localized to smaller regions.The decreasing temperature in the domain is likely a results of insufficient flow time. This was further confirmed, as a coarse mesh containing $\approx$ 80e+03 cells was able to simulate 30 s of flow time with a deviation of only 21.6%. Simulations using the eddy-dissipation model were found to have a deviation of 37.3% and 38.3%, while simulations using finite rate/eddy dissipation had a much larger deviation of 47.7%, compared to the experimental results.
Lastly, it is concluded that Ansys Fluent is capable of delivering reasonable results in multiphase-combustion simulations, without the use of UDFs. The deviations of the simulations are not caused by a lack of UDFs, but rather a result of the mesh and limited computational time.

9 Further Work

Future studies could focus on systematically varying the levels of O_2 and analyze the resulting changes in system performance and emissions, considering both fresh and recycled oxygen sources. Additionally the incorporation of limestone is commonly used in CFB systems to control SO_x emissions through in-situ desulfurization. Investigating the effect of limestone in the GHG emissions and especially SO_x could be of great interest, both for companies and for academic research. Combining the above-mentioned, an economical study could conclude feasibility of both the addition of limestone and the use of oxy-fuel combustion. While this study intentionally avoided the use of UDFs, incorporating them could lead to significantly better simulation capabilities, since it allows to model specific physical phenomena. Alternatively, other modeling approaches could be utilized, such as LES that is able to capture finer details of the flow. This would, however, require significantly more computational resources or time. Furthermore, future studies could look further into the development of a steady simulation in order to reduce the computational time. This could additionally be compared to transient simulation to establish a suitable simulation time for transient simulations, in order to obtain results where the system has reached a state resembling the steady state solution.

Bibliography

[1] Shiyuan Li et al. "Influence of operating parameters on N2O emission in O2/CO2 combustion with high oxygen concentration in circulating fluidized bed". In: *Applied Energy 173* (2016). DOI: 10.1016/j.apenergy.2016.02.054.

[2] Jinrao Gu, Wenqi Zhong, and Aibing Yu. "Three-dimensional simulation of oxy-fuel combustion in a circulating fluidized bed". In: *Powder Technology 351* (2019). DOI: 10.1016/j.powtec.2019.04.008.

[3] European Comission. *2050 long-term strategy*. 2024. URL: https://climate.ec.europa.eu/eu-action/climate-strategies-targets/2050-long-term-strategy_en.

[4] Energi-og Forsyningsministeriet Klima. *Klimaprogram 2023*. 2023. ISBN: 978-87-94224-61-1.

[5] EDGAR/JRC. *Distribution of carbon dioxide emissions worldwide in 2022, by sector*. 2023. URL: https://www.statista.com/statistics/1129656/global-share-of-co2-emissions-from-fossil-fuel-and-cement/.

[6] EEA. *Annual greenhouse gas emissions in the European Union (EU-27) from 1990 to 2021, by sector*. 2024. URL: https://www.statista.com/statistics/1171183/ghg-emissions-sector-european-union-eu/.

[7] Toby Lockwood. *Techno-economic analysis of PC versus CFB combustion technology*. 2013. ISBN: 978-92-9029-546-4.

[8] Prabir Basu. *Circulating Fluidized Bed Boilers Design, Operation and Maintenance*. 2015. ISBN: 978-3-319-06172-6.

[9] Qing Wang, Jianbo Xiao, and Hongpeng Liu. "CFD simulation of hydrodynamics on the dense zone on a 65 t/h oil shale-fired highlow bed CFB boiler". In: *Powder Technology 249* (2013). DOI: 10.1016/j.powtec.2013.07.037.

[10] Li Peng et al. “2.5D CFD simulations of gassolids flow in cylindrical CFB risers”. In: *Powder Technology 291* (2015). DOI: 10.1016/j.powtec.2015.12.018.

[11] Thanh D.B. Nguyen et al. “CFD simulation with experiments in a dual circulating fluidized bed gasifier”. In: *Computers and Chemical Engineering 36* (2012). DOI: 10.1016/j.compchemeng.2011.07.005.

[12] Mukesh Upadhyay and Jong-Ho Park. “CFD simulation via conventional Two-Fluid Model of a circulating fluidized bed riser: Influence of models and model parameters on hydrodynamic behavior”. In: *Powder Technology 272* (2015). DOI: 10.1016/j.powtec.2014.12.011.

[13] Musango Lungu et al. “Effect of bed thickness on a pseudo 2D gas-solid fluidized bed turbulent flow structures and dynamics”. In: *Powder Technology 336* (2018). DOI: 10.1016/j.powtec.2018.06.028.

[14] L.M. Armstrong, K.H. Luo, and S. Gu. “Two-dimensional and three-dimensional computational studies of hydrodynamics in the transition from bubbling to circulating fluidised bed”. In: *Chemical Engineering Journal 160* (2010). DOI: 10.1016/j.cej.2010.02.032.

[15] Mukesh Upadhyay et al. “Experiment and multiphase CFD simulation of gas-solid flow in a CFB reactor at various operating conditions: Assessing the performance of 2D and 3D simulations”. In: (2020). DOI: 10.1007/s11814-020-0646-7.

[16] Muhammad Adnan et al. “Comparative CFD modeling of a bubbling bed using a EulerianEulerian two-fluid model (TFM) and a Eulerian-Lagrangian dense discrete phase model (DDPM)”. In: *Powder Technology 383* (2021). DOI: 10.1016/j.powtec.2021.01.063.

[17] Adnan Muhammad, Nan Zhang, and Wei Wang. “CFD simulations of a full-loop CFB reactor using coarse-grained EulerianLagrangian dense discrete phase model: Effects of modeling parameters”. In: *Powder Technology 354* (2019). DOI: 10.1016/j.powtec.2019.06.016.

[18] Tingwen Li, Jean-François Dietiker, and Lawrence Shadle. “Comparison offull-loopandriser-onlysimulations for apilot-scalecirculating fluidized bedriser”. In: *Chemical Engineering 120* (2014). DOI: 10.1016/j.ces.2014.08.041.

[19] Yujian Lu et al. “Verification of optimal models for 2D-full loop simulation of circulating fluidized bed”. In: *Advanced Powder Technology 29* (2018). DOI: 10.1016/j.apt.2018.07.024.

[20] Sirpa Kallio, Juho Peltola, and Timo Niemi. “Modeling of the time-averaged gassolid drag force in a fluidized bed based on results from transient 2D EulerianEulerian simulations”. In: *Powder Technology 261* (2014). DOI: 10.1016/j.powtec.2014.04.045.

[21] Tingwen Li, Sreekanth Pannala, and Mehrdad Shahnam. “CFD simulations of circulating fluidized bed risers, part II, evaluation of differences between 2D and 3D simulations”. In: *Powder Technology 254* (2014). DOI: 10.1016/j.powtec.2014.01.022.

[22] Timo Niemi and Sirpa Kallio. “Modeling of conversion of a single fuel particle in a CFD model for CFB combustion”. In: *Fuel Processing Technology 169* (2017). DOI: 10.1016/j.fuproc.2017.10.010.

[23] Wu Zhou et al. “CFD modeling of oxy-coal combustion in circulating fluidized bed”. In: *International Journal of Greenhouse Gas Control 5* (2011). DOI: 10.1016/j.ijggc.2011.08.006.

[24] Wojciech P. Adamczyk et al. “Generation of data sets for semi-empirical models of circulated fluidized bed boilers using hybrid Euler-Lagrange technique”. In: *Energy 143* (2017). DOI: 10.1016/j.energy.2017.10.029.

[25] Ying Wu et al. “Effects of gas-solid drag model on Eulerian-Eulerian CFD simulation of coal combustion in a circulating fluidized bed”. In: *Powder Technology 324* (2017). DOI: 10.1016/j.powtec.2017.10.013.

[26] Ying Wua et al. “Three-dimensional CFD simulation of oxy-fuel combustion in a circulating fluidized bed with warm flue gas recycle”. In: *Fuel 216* (2018). DOI: 10.1016/j.fuel.2017.12.042.

[27] Wojciech P. Adamczyk et al. “Numerical simulations of the industrial circulating fluidized bed boiler under air- and oxy-fuel combustion”. In: *Applied Thermal Engineering 87* (2015). DOI: 10.1016/j.applthermaleng.2015.04.056.

[28] Wojciech P. Adamczyk et al. “Modeling oxy-fuel combustion in a 3D circulating fluidized bed using the hybrid Euler-Lagrange approach”. In: *Applied Thermal Engineering 71* (2014). DOI: 10.1016/j.applthermaleng.2014.06.063.

[29] LI Kun et al. "Comparison of Fully 3-D, Simplified 3-D and 2-D Numerical Simulations on a Circulating Fluidized Bed Boiler". In: *Journal of Thermal Science 32* (2023). DOI: 10.1007/s11630-023-1879-7.

[30] ANSYS inc. *Ansys Fluent Theory Guide*. Release 2024 R1. 2024.

[31] H.K. Versteeg and W. Malalasekera. *An Introduction to Computational Fluid Dynamics*. 2nd. ISBN: 978-0-13-127498-3. Pearson Education Limited, 2007.

[32] IdealSimulations. *Turbulence Models In CFD*. 2020. URL: https://www.idealsimulations.com/resources/turbulence-models-in-cfd/.

[33] Hookyung Lee, Sangmin Choi, and Bongkeun Kim. "Understanding Coal Gasification and Combustion Modeling in General Purpose CFD Code". In: *, Vol.15, No.3, pp.15-24(2010)* (2010). URL: https://www.researchgate.net/publication/264173264_Understanding_Coal_Gasification_and_Combustion_Modeling_in_General_Purpose_CFD_Code.

[34] Nist Chemistry Web book. *Methane*. 1998. URL: https://webbook.nist.gov/cgi/cbook.cgi?ID=C74828&Mask=1&Type=JANAFG&Table=on.

[35] CFD Online. *CourantFriedrichsLewy condition*. 2012. URL: https://www.cfd-online.com/Wiki/Courant%E2%80%93Friedrichs%E2%80%93Lewy_condition.

[36] P. J. Roache. "Perspective: A Method for Uniform Reporting of Grid Refinement Studies". In: *Ecodynamics Research Associates, inc.* (1994).

A Appendix

A.1 Injection File Script

```
% Parameters
num_particles = 150000; %Number of particles/parcels

% Cylinder dimensions
radius = 0.035; %Radius of the cylinder (m)
height = 1.5; %Height of the cylinder (m)

% Generate random points within the cylinder
theta = 2*pi*rand(1, num_particles); %Random angle
r = radius*sqrt(rand(1, num_particles)); %Random radius
x = r.*cos(theta); %x-coordinate within the cylinder
y = (height-0.001)*rand(1, num_particles) + 0.001; %y-coordinate within the
    cylinder
z = r.*sin(theta); %z-coordinate within the cylinder

% Other parameters
u = zeros(1, num_particles); %Velocity in x-direction
v = zeros(1, num_particles); %Velocity in y-direction
w = zeros(1, num_particles); %Velocity in z-direction
diameter_range = 0.002;
temperature = 300; %Temperature (K)
injection = "injection:0";
m_1 = 4.502687673; %9.189;
t = 1*10^-8;
massflow = (m_1/t)/num_particles;
rho = 2600;


% Values
%diameter = rand(1, num_particles) * (diameter_range(2) - diameter_range(1)) +
    diameter_range(1);
```

```
30 diameter_array = repmat(diameter, 1, num_particles);
31 temperature_array = repmat(temperature, 1, num_particles);
32 massflow_array = repmat(massflow, 1, num_particles);
33 injection_array = repmat(injection, 1, num_particles);
34 name = (1:num_particles)'; %Particle identification numbers
35
36
37 % Write to file
38 fileID = fopen('riser_particle_injection.inj', 'w');
39 for i = 1:num_particles
40     fprintf(fileID, '((%f %f %f %f %f %f %f %f) %s)\n', ...
41         x(i), y(i), z(i), u(i), v(i), w(i), diameter_array(i), temperature_array
            (i), massflow_array(i), injection);
42 end
43 fclose(fileID);
44 disp('Text file "riser_particle_injection.inj" generated successfully.');
```

B Appendix

B.1 Early simulations and diverged simulations

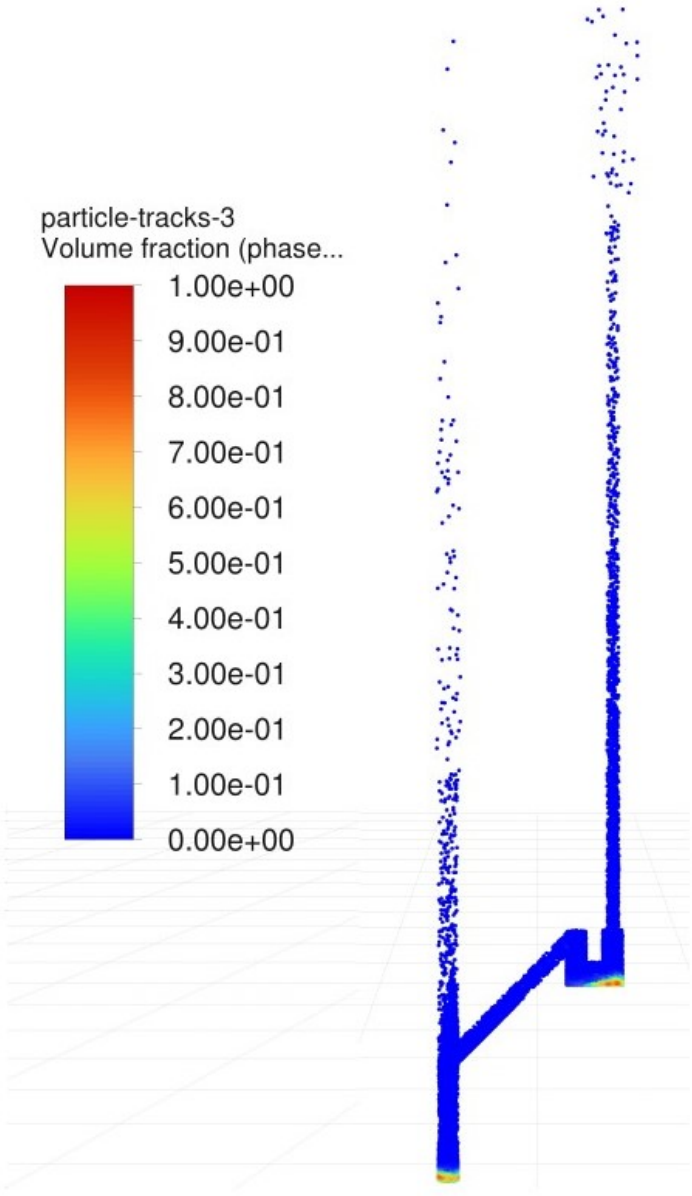

Figure B.1: Early simulation without turbulence model and 500000 particles

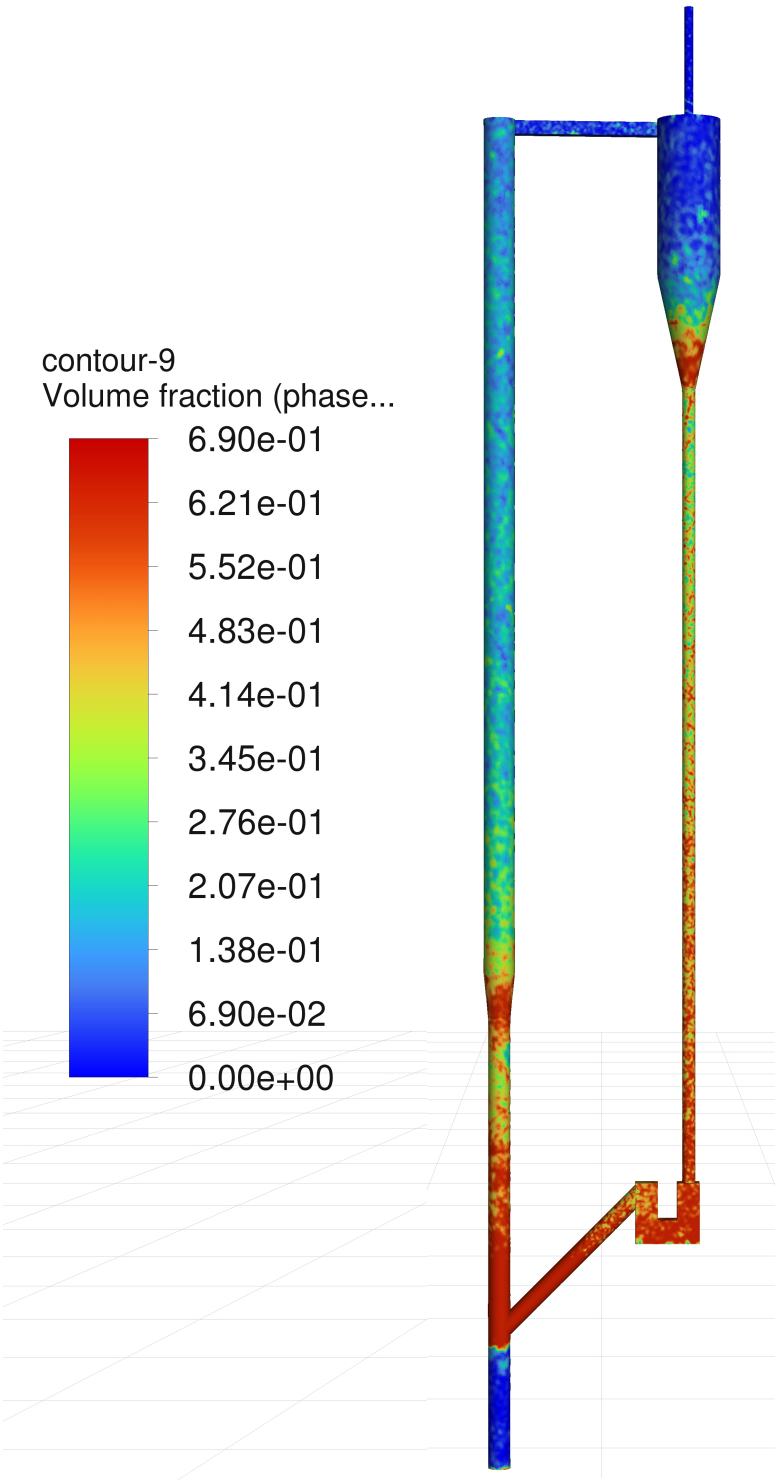

Figure B.2: No combustion with ddpm and without DEM after 6000 iterations in steady simulation.

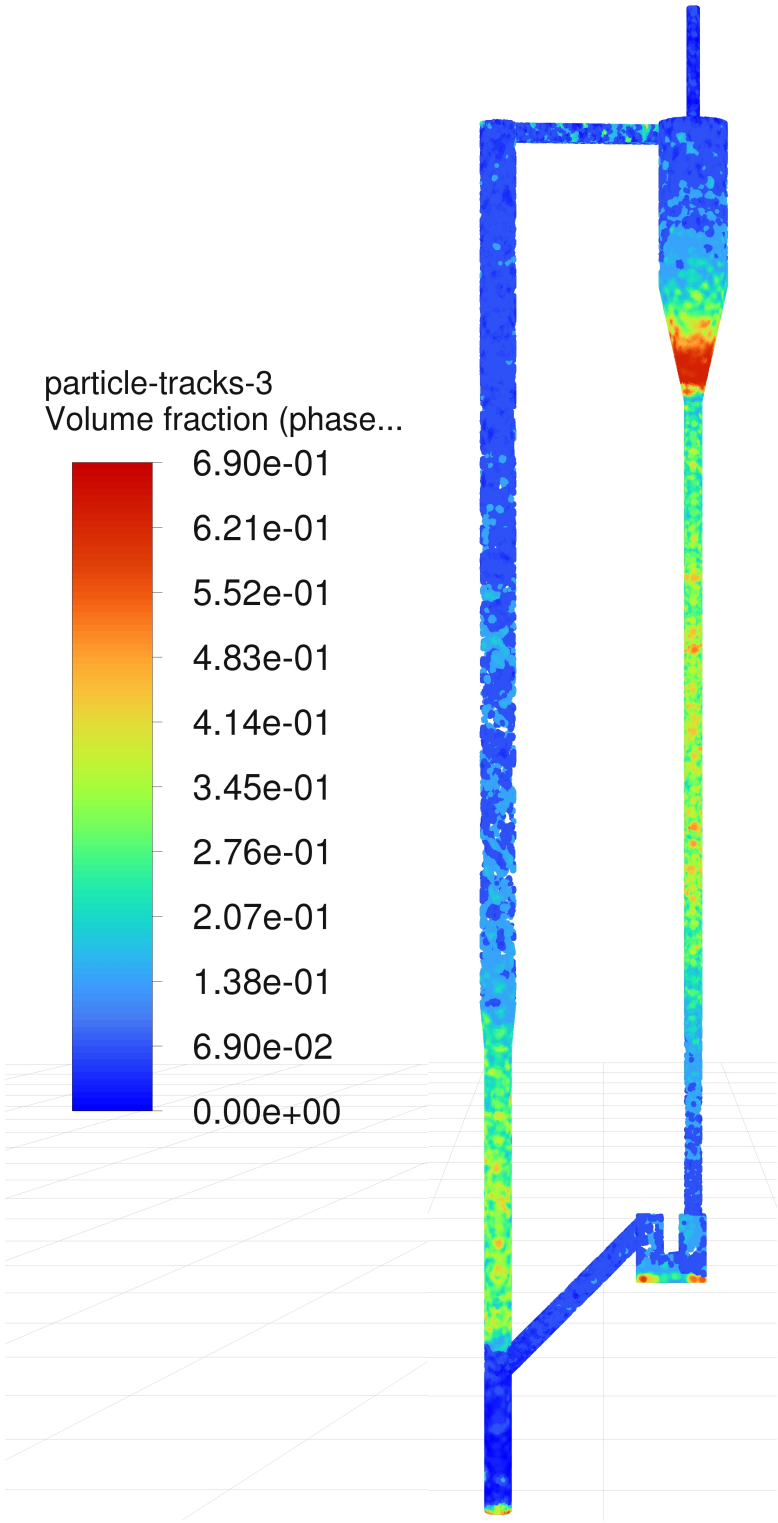

Figure B.3: No combustion with ddpm and without DEM in steady simulation.

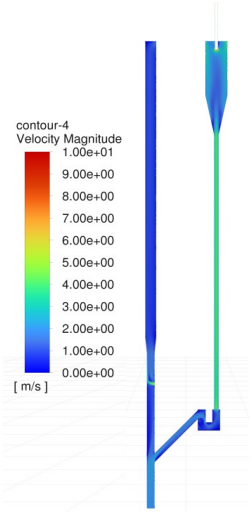

Figure B.4: Cold simulation with turbulence colored by the velocity magnitude.

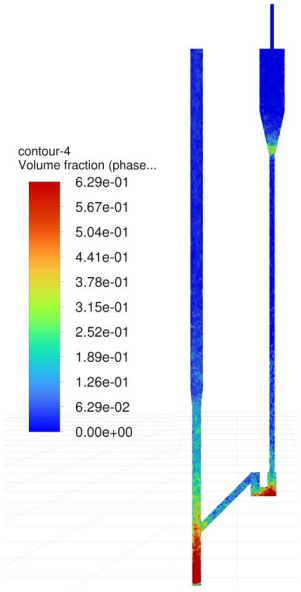

Figure B.5: Cold simulation with turbulence, DDPM and DPM colored by volume fraction of particulate phase.

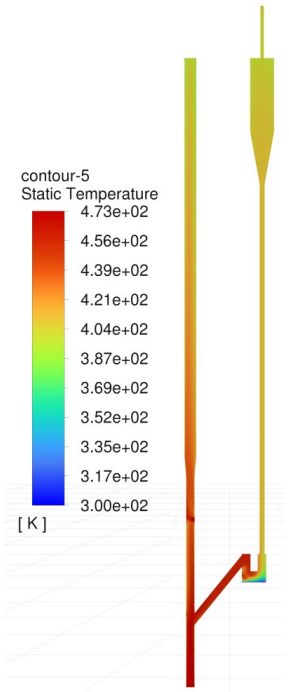

Figure B.6: Hot simulation with turbulence colored by the static temperature.

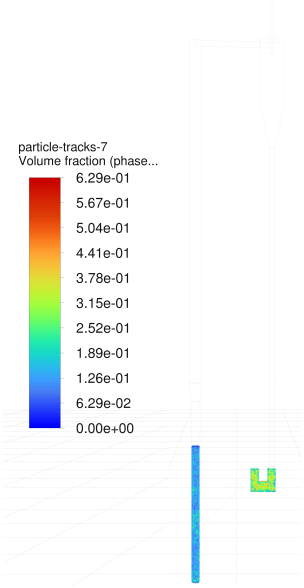

Figure B.7: Particle tracking coloured after volume fraction.